University of Alberta

Fabrication of Nanostructures by Low Voltage Electron Beam Lithography

by

Adegboyega Paul Adeyenuwo

A thesis submitted to the Faculty of Graduate Studies and Research
in partial fulfillment of the requirements for the degree of

Master of Science
in
Micro-Electro-Mechanical Systems (MEMS) and Nanosystems

Department of Electrical and Computer Engineering

Spring 2012
Edmonton, Alberta

To my parents:

You mean everything to me and will be the best parents I could ever have!

Abstract

Electron Beam Lithography (EBL) is a powerful tool for structuring materials at the deep nanoscale. Modeling and simulation of electron-beam interactions at this length scale is vital to understanding and optimizing nanofabrication using EBL. The low to high voltage (5 keV – 100 keV) regimes of EBL have been studied for decades. However, the ultra-low regime (< 5 keV) provides an opportunity to further rationalize the understanding of this powerful technique and explore its applications. The ultra-low voltage regime was studied using (poly) methyl-methacrylate (PMMA) as the resist, and important metrics at this regime such as dose windows, exposure sensitivity and dose variation with exposure energy are explored. An application of low voltage EBL is presented to develop a process for pattern density multiplication in a single step. Density multiplication was demonstrated for arrays of nanostructures using a combination of experiments and simulation. This approach increased the areal density of the lithographically patterned arrays of dots and lines by a factor of approximately 2 in a single exposure and development step. This application is not only interesting from a technological perspective, but also demonstrates the power of a combined experimental and simulation optimization strategy.

Acknowledgement

I would like to thank my supervisors, Prof. Steve Dew and Dr. Maria Stepanova for giving me the opportunity to work in their research group and also on fascinating projects, which has taught me a lot in both theoretical knowledge and hands-on laboratory experiments. Working on this team has also enabled me to meet great people and carry out research work in excellent facilities, which I really do appreciate!

I acknowledge the help of all the team members who showed me some of the laboratory processes that were already in use when I joined the group: Jiang Chen, Mohammad Ali Mohammad and Taras Fito who was my go-to resource when I first started to work on our simulator project. It has been very nice working with all of you!

I gratefully acknowledge the NanoFab staff and Daniel Salamon at the NINT for his generous help and directions for my electron microscopy sessions. A big thank you to all of you!

Lastly, I would like to thank my family and friends for their endless love, support and prayers.

Table of Contents

List of Tables

List of Figures

List of Abbreviations

EBID - electron-beam-induced deposition

EBL - electron beam lithography

EUVL - extreme ultraviolet lithography

HSQ - hydrogen silsesquioxane

IBL - ion beam lithography

IPA - isoprapanol alchohol

MEMS - micro-electro-mechanical systems and nanosystems

MIBK - methyl isobutyl ketone

NEMS - nano-electro-mechanical systems and nanosystems

NIL - nanoimprint lithography

PMMA - polymethylmethacrylate

SEM - scanning electron microscopy

SPL - scanning probe lithography

XRL - X-ray lithography

1 Introduction

The unprecedented boom being experienced by the semiconductor and related microfabrication industry will likely continue for several years down the road with the industry seeing significant growth across all major end-use sectors including consumer, automotive, computer, industrial, communications and government applications. In a recent release, the Semiconductor Industry Association announced a 14% year-to-year growth of the semiconductor industry. [1, 2, 3] This growth is attributable to the increased use of semiconductor technology in a wider range of electronic devices. [2] This unrelenting demand [3] will, for the foreseeable future, continually require smaller dimensions of devices [4] for photonics, information storage and microprocessor applications. This trend necessitates the continual invention and improvement of new techniques to fabricate dense patterns of nanostructures on larger chip areas.

Nanofabrication is the study and application of top-down or bottom-up fabrication techniques to the generation of nanoscale structures with dimensions of less than 100 nm. [5] These structures can be generated for studying the behavior of nanoscale materials and processes or as a complex pattern to form novel devices or their components. Nanofabrication is vital to many if not most fields of nanotechnologies. [5]

Top-down fabrication techniques involve the fabrication of structures from a bulk material by removing of or adding to the bulk material nanoscale patterns. [5] In this approach, the parts that make up the device or component are usually patterned in

several layers with each step involving an addition, removal or a change in material properties (e.g. exposure of a resist material by electrons). The top-down approach has proven to be a critical tool for the sustained evolution of the semiconductor and associated industries spanning analog, digital and memory integrated circuits (ICs), information storage, photonics, microfluidics and micro- and nano-electro-mechanical systems and nanosystems (MEMS and NEMS). [5]

Bottom-up fabrication techniques comprise strategies to manipulate or build structures, components, devices and systems by directed/self-assembly of atoms, molecules or supramolecular elements. [5] Synthesis of these types of structures uses naturally occurring physical and chemical processes in various systems including solid surfaces, polymers, and biosystems. Self-assembly of block copolymers is an example of intensely exploited bottom-up nanostructuring. [5, 6, 7, 8] The applications are broad, from nano-composites to bio-medical, chemical and physical sensors and actuators.

Lithography is regarded as the most fundamental top-down fabrication process of semiconductor devices and is critical in micro and nanofabrication in order to progressively produce the high-density integrated circuits that power the ubiquitous electronic devices of today and tomorrow. Optical lithography, [6] the most mature of these technologies, can also achieve sub 100 nm resolution using enhancement techniques such as deep UV sources, high numerical aperture optics, liquid immersion, phase shift masks and optical proximity correction. However, as device dimension have shrunk far below the wavelengths of visible UV light, it becomes impossible to extend optical lithography further into the deep nanoscale.

For this, several lithographic approaches have been used to achieve nanoscale fabrication of features including electron beam lithography [9, 6, 10] (EBL), ion beam lithography (IBL), extreme ultra-violet lithography [6] (EUVL), nanoimprint lithography [6] (NIL), scanning probe lithography [6] (SPL) x-ray lithography [6] (XRL), and electron-beam-induced deposition (EBID). [5] In this thesis, the focus is on nanofabrication was using EBL as the most flexible and mature of these options.

EBL has been the major direct-write technique to controllably fabricate structures at the nanoscale for decades. [11, 12, 13] The technique involves bombarding a chemical film (resist) with a beam of electrons (exposure) and selectively removing the exposed or unexposed areas of the resist with a solvent (development). [11, 9] This technique is capable of creating high resolution structures in the resist material which can then be transferred to the substrate or underlying material in a subsequent step such as etching.

The major advantage of EBL is its capability to circumvent the limitations imposed by the diffraction limit of light in optical lithography and therefore, generate patterns in the nanometer regime. EBL serves numerous purposes including photomask-making for use in optical and nanoimprint [14] lithography, bit-patterned media for high density recording, [15, 16] high resolution templated self-assembly, [7, 17] photonic [18] and nanoelectronic [19] devices, research and development. EBL is a serial writing technique and therefore is limited in throughput. Therefore, in order to write a pattern that covers an entire wafer, it may take several hours or days. For example, defining of a master template for a

95-mm patterned media disk at 1 terabit per square inch (Tb/in^2) would take more than a month. [20] In spite of these limitations, EBL delivers a resolution sufficient to write features down to 10 nm dimensions and less. [21, 22] Furthermore, very high dimensional control ensures that reproduction of the same feature size with the same tolerance and position accuracy across an entire wafer and wafer-to-wafer is possible. The value added by the EBL is high and could present a viable business model where, for example, a high resolution sensor fabricated using EBL could be sold for $1,000s as opposed to a model where billions of transistors could be sold for much less.

An alternative approach strives to improve EBL throughput by parallelizing [23, 24, 25] the process of exposure. For example, MAPPER [23] is an initiative to develop a multi-beam micro-column system [23] that is capable of using 10,000 concurrent writing beams. [23, 24, 25] An array of micro-columns opens up a huge potential for the application of EBL for volume production in the microelectronics (IC) industry. The current system developed by MAPPER [23] uses low voltage EBL at 5 kV. Further exploration of low voltages is relevant and a huge boost to the potential of EBL as a major technology for lithography at the nanoscale.

In my research, I focus on the ultra-low voltage regime to attain a fundamental understanding of this aspect of EBL, the optimal conditions to reproducibly fabricate dense arrays of nanostructures, characterize the features fabricated and study the behavior of the exposure tools at this limit of its capacity. This thesis describes my contribution to ongoing research in the Nanofabrication Group at the University of Alberta and the National Institute for Nanotechnology (NINT).

In the course of my participation in the group, I have carried out frontier research and developed applications of low voltage electron beam lithography, particularly at 1 keV and 2 keV. The work includes the application of the ultra-low voltage EBL to density multiplication of nanostructures. In addition, I contributed to the development of an electron beam simulation software for modeling the process of nanofabrication of structures, participated in testing and documentation of the software and used the simulator in my experimental work.

In the thesis, Chapter 2 reviews the literature on electron beam lithography, including instrumentation, electron beam resists, process parameters and introduces the concept of dose windows. It also reviews literature on electron beam modeling and simulation, available simulator software tools, including the NINT EBL simulator and the models of exposure and development employed in the software.

Chapter 3 discusses the methodology that was employed during my research. The experimental equipment used, sample preparation processes, and major steps in EBL processing such as exposure, development, characterization as well as the simulator development and testing are discussed.

Chapter 4 presents the results of experimental research and optimization of the conditions of ultra-low voltage EBL, sensitivity, the applicable windows for fabricating nanostructures, comparative analysis of dose windows for 1 keV and 2 keV and metrology of fabricated nanostructures

Chapter 5 presents results of the application of low-voltage EBL to density multiplication in PMMA and discusses the experiments, modeling and results obtained.

Chapter 6 gives a conclusion of the work done throughout the thesis and comments about further research that could be performed in the future.

2 Literature Review

2.1 **Electron Beam Lithography**

The rapid pace of miniaturization and integration of devices fabricated on a silicon chip requires continuous advances in next generation lithographic technologies. With the recognition of the fact that optical lithography will soon approach a limit of economic viability and resolution limit, [26] it is crucial that alternative lithographic technologies be developed. According to the 2010 Semiconductor Industry Association (SIA) International Technology Roadmap for Semiconductors (ITRS), technical solutions to the challenges of lithography must ensure that costs remain economical with design and process developments. [27] This thesis details research work aimed at process improvements and chronicles fundamental experimental research to better understand and improve the electron beam lithography process at low voltages, particularly 1 keV and 2 keV, as well as the performance of the exposure tool at this limit of capacity.

Electron Beam Lithography (EBL) is the standard [11, 10] and major direct-write technique [9] for high-resolution, [10] and controllable fabrication of nanoscale features. [9, 12]

The EBL process is comprised of spin-coating a radiation sensitive layer (e-beam resist) onto a substrate and exposing the resist by a steerable beam of electrons which causes a chemical change in the resist such as chain scissioning in a positive tone polymer resist such as polymethylmethacrylate (PMMA). The exposed regions of the resist are subsequently dissolved faster in a suitable

solvent (developer) and are therefore removed. [11, 9] The resulting pattern can be employed for further processing steps, such as lift-off, or etching. [11]

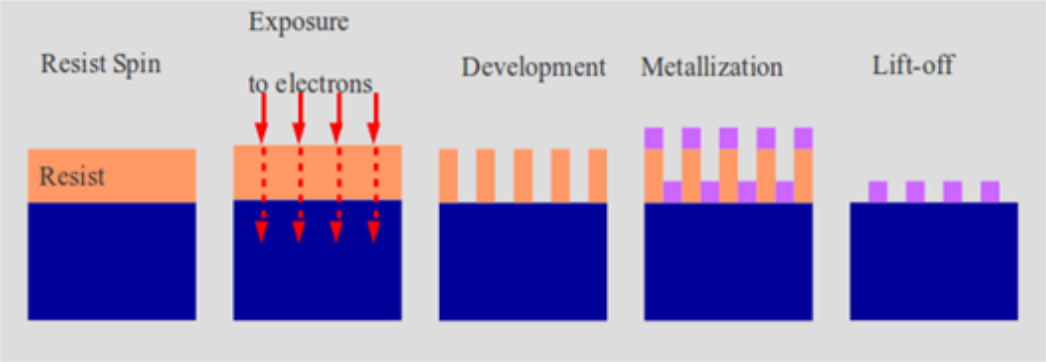

Figure 1: Major steps in EBL [11]

The limitations of EBL resolution are related to undesired exposure of the resist at locations away from the point of impact of the electrons due to electron scattering in the resist. Electron stopping results from a series of many collisions, each involving a small energy transfer. As a result, the primary incident beam is broadened by forward scattering. When the electrons are deflected back from the substrate after travelling through the resist, the resulting backscattered electrons expose adjacent locations, resulting in the so called proximity effect. Both primary and backscattered electrons also generate secondary electrons in the resist which can travel short distances before exposing the resist at a point removed from the initial incidence. These limitations, individually or collectively, challenge the resolution achievable by EBL.

On the one hand, while usage of EBL at higher voltages of 10 keV to 30 keV produces high-resolution structures somewhat easily as a result of reduced

forward scattering, it has the disadvantage of being more expensive, having a lower throughput due to the higher electron dose required for exposure and causing unwanted substrate damage due to deep penetration of electrons in the resist. On the other hand, ultra-low voltage electrons in the 1-3 keV regimes deposit most of their energy within the resist resulting in less substrate damage and decreasing dramatically the proximity effect [28, 29] as well as requiring significantly lower doses roughly in proportion to the accelerating voltage. [29] The strong forward scattering of low energy electrons, which is routinely believed to be the major resolution-limiting factor, creates undercut profiles in the resist which may be used as re-entrant profiles in lift-off processing. [28, 30]

Fabrication of nanostructures using electron beam lithography (EBL), especially at voltages of 3 keV and greater, is well characterized and broadly used. [9, 28, 30] For positive-tone resists such as polymethylmethacrylate (PMMA), the electron bombardment causes scission of the main chain molecular bonds of the polymer. The polymer is broken into several fragments of reduced molecular weights and increased solubility in certain solvents. During development, the fragmented exposed areas of the resist dissolve, PMMA thus responding as a positive-tone resist. [11, 30, 31, 21, 22, 32, 33, 34, 35] However, if PMMA is overexposed at several times higher dose than required for positive-tone behavior, cross-linking of PMMA molecules occur rather than scission. [12, 31, 34, 35, 36, 37, 38, 39] This decreases solubility. During development, patterns of overexposed PMMA remain at exposed locations, thus behaving as a negative-tone resist. In a number of works, the high dose electron beam irradiation of PMMA has been proposed to result from a

carbonization process [12, 34, 35, 36, 37, 38, 39] rather than a cross linking of the PMMA fragments. However, there is no doubt that in appropriate exposure regimes, PMMA can behave as both a positive-tone and negative-tone resist. In the light of the allusions made in, [22, 40, 41] it is quite natural to assume that it may be possible to fabricate both negative-tone and positive-tone patterns in PMMA in a single exposure and development process step. This characteristic of PMMA is also exploited in this thesis.

2.2 **Instrumentation**

The EBL technique requires that a source generates electrons, which are then focused into a beam and accelerated at a desired voltage to impinge on a substrate. The electrons are generated by the electron gun, which comprises a cathode and several beam-shaping and focusing electrodes. Figure 1.2 shows the internal arrangement of the main components of an EBL system. The beam of emitted electrons is accelerated up to a required voltage, typically in the range of 10 keV to 30 keV, between the cathode and the electrostatic plates that function as the anode. Various electric and magnetic fields align, shape, focus, blank, and deflect the beam as it is accelerated to bombard the wafer. The entire column from electron gun through the wafer stage is kept under vacuum so that the electron paths are not unduly affected by collisions with gas molecules. [42]

Under the control of a computer, the drive signals for the various electrodes are read and executed from a program, which provides the basic scanning instructions. By employing signal processing, the computer can adjust the beam

motion to correct distortion and aberration in the several chip fields as well as control the wafer stage motion. [42]

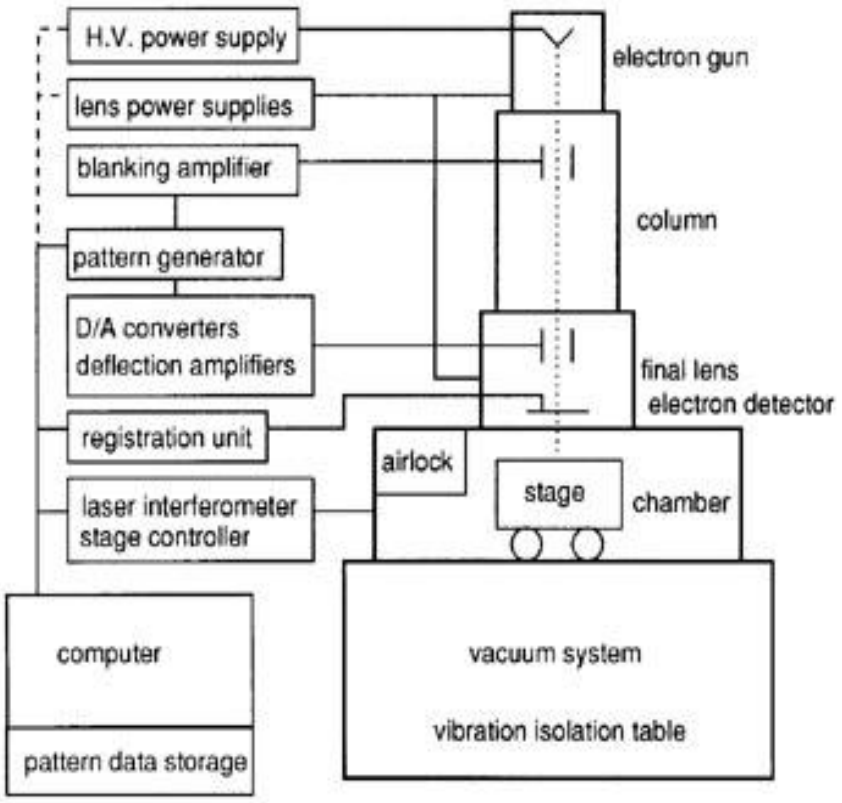

Figure 2: Block diagram showing the major components of a typical electron beam lithography system [43] [Reproduced by permission of SPIE]

2.3 **Electron Beam Resist**

Electron beam resist is a material made up of an electron sensitive compound, sensitizer and a casting solvent which, on exposure to radiation, changes in structure. [6, 42] The resist serves as the recording and transfer media for electron beam lithography. [43] The resist could be a positive tone resist or a negative tone resist. In a positive resist, exposure to radiation causes rupture or scission in the main and side chains of the polymer. [6] As a result, the exposed resist becomes

more soluble in a developing solution. Examples of positive tone e-beam resists are polymethylmethacrylate (PMMA) [6, 43] and ZEP-520. [44, 45] A negative resist upon exposure to radiation undergoes a series of electron-activated reactions, which strengthen the material by cross-linking thereby making it less soluble in developers. [6] Examples of negative resists are Microposit SAL601, [6] hydrogen silsesquioxane (HSQ), [46] various calixarenes and hexaacetate p-methylcalixarene, (MC6AOAc). [47, 48]

There are numerous other e-beam resists produced for mask making and direct-write applications. The bombardment of polymers by electrons generally causes the bonds to break and, in principle, any polymer can function as a resist. However, the important considerations include selectivity, tone, resolution, etching resistance [6] and line edge roughness. [49]

PMMA was one of the first materials developed for EBL and is usually available in two high molecular weight forms of 496K or 950K in a casting solvent such as cholorobenzene or anisole [43]. It is a popular example of an inexpensive e-beam resist with a high resolution capability and a moderate glass transition temperature. [6] The PMMA is spun onto a substrate to achieve the desired thickness, and then soft baked at 175 °C to drive off the casting solvent before being exposed to the electron beam. Main-chain scission occurs [50] under exposure to electrons breaking the polymer into smaller fragments. [11, 43, 13]

2.4 **Process Parameters and Windows**

Electron beam lithography involves a complex interplay of several process parameters and deviations from optimized conditions result in significant variations in the resulting morphology. The practical significance of the understanding of the complex interactions of these parameters to a process engineer, for example, is gaining the knowledge of how much margin or tolerance a specific EBL process can afford before failure. This obviously has the advantage of saving a lot of money and time for a process that is inherently resource intensive.

Figure 3 shows SEM images of 30, 40, 50, and 70 nm pitch gratings fabricated in a 65 nm thick PMMA layer, with 10 keV electrons at various doses as indicated, and developed for 5 s in a MIBK:IPA 1:3 solution at room temperature. [11, 9] The figure demonstrates the variations of grating morphologies that are generated with changes in the process parameters. For example, comparing column-wise morphologies, higher density gratings constrict the process window such that while 70 nm grating structures in Figures 3(d), (h), (l), (p) could be generated at all dose conditions, the quality of nanostructures decreases for 50 nm, 40 nm and 30 nm respectively where it was impossible to generate a grating pattern under the given process conditions. Also, by changing only two process parameters, dose and pitch, several nanostructure morphologies are observed in the images: under-exposure, good exposure, over-exposure, miscellization and collapse. [11, 9, 30]

Under-exposure occurs when the electron dose is insufficient to clear the resist material down to the substrate as shown in Figure 4 (a) while over-exposure

occurs when the excessive resist material is removed from exposed areas as a result of an electron dose higher than required leading to pattern collapse as shown in Figure 4 (c). At much higher doses, complete removal of the resist material occurs. [11, 9, 30] The region of good exposure exists between these two extremes where the resist is cleared down to the substrate but the walls of the remaining resist material are not degraded by excessive removal to cause pattern collapse. This regime is shown as Figure 4 (b).

Figure 5 shows a plot of the various regions of surface morphologies summarizing the experimental result of Figure 3: underexposure, good exposure, over-exposure, miscellization and collapse. [11, 9, 30]

The process parameters in EBL cover both exposure and development steps of the process. For exposure, the parameters are: exposure energy (or voltage), resist thickness, pattern density (pitch/spacing) and electron dose. For development, the process parameters comprise duration (time) and development temperature. [11, 9, 30] These factors must be co-optimized for a given resist, substrate and developer. While several of these factors have been investigated extensively, co-optimizing these factors to understand their relationships and process windows is a complex task, particularly at ultra-low energies of 1 keV and 2 keV. The concept of dose window is a simple yet powerful approach to gaining an understanding of how electron dose at a specified development time at and energy determines the resulting morphology in EBL. Generally, it gives a graphical plot of specific process conditions for which a quality pattern can be generated such as shown in Figure 5. [11, 9, 30] The approach of identifying applicable dose windows is applied in

this thesis to find the optimal conditions of PMMA processing at ultra-low exposures.

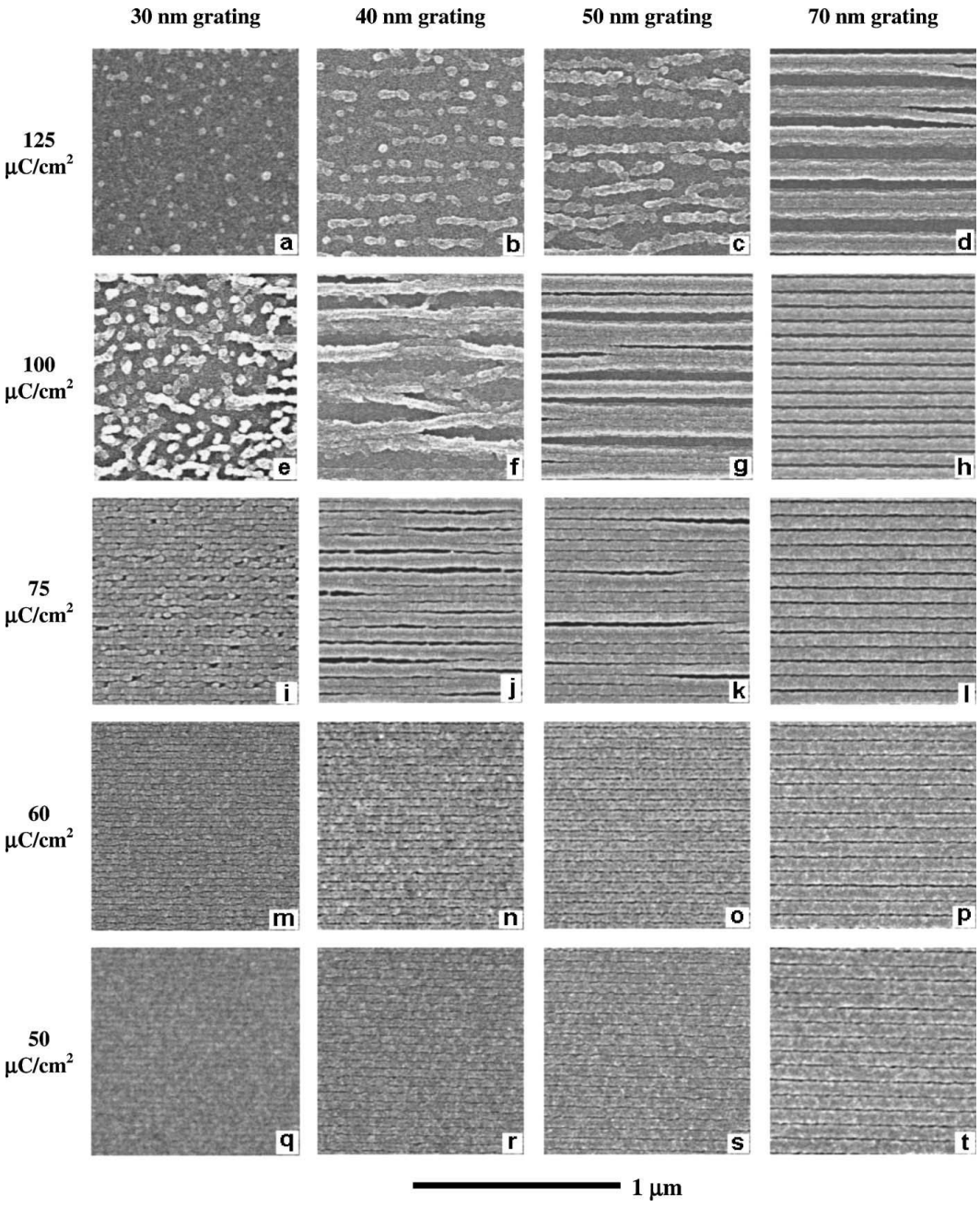

Figure 3: SEM images of 30, 40, 50, and 70 nm gratings fabricated in a 65 nm thick PMMA layer at 10 keV using various doses and developed for 5 sec in a MIBK:IPA 1:3 solution at room temperature [11, 30]

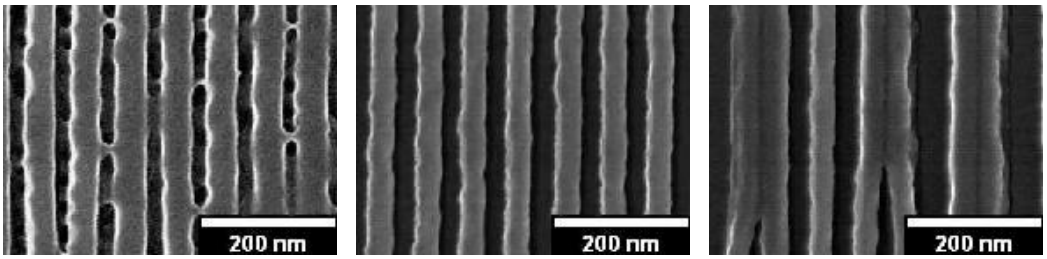

(a) (b) (c)

Figure 4: Plan view SEM micrographs of (a) under-exposed, (b) good exposure, and (c) collapsed gratings in PMMA [11, 9, 30]

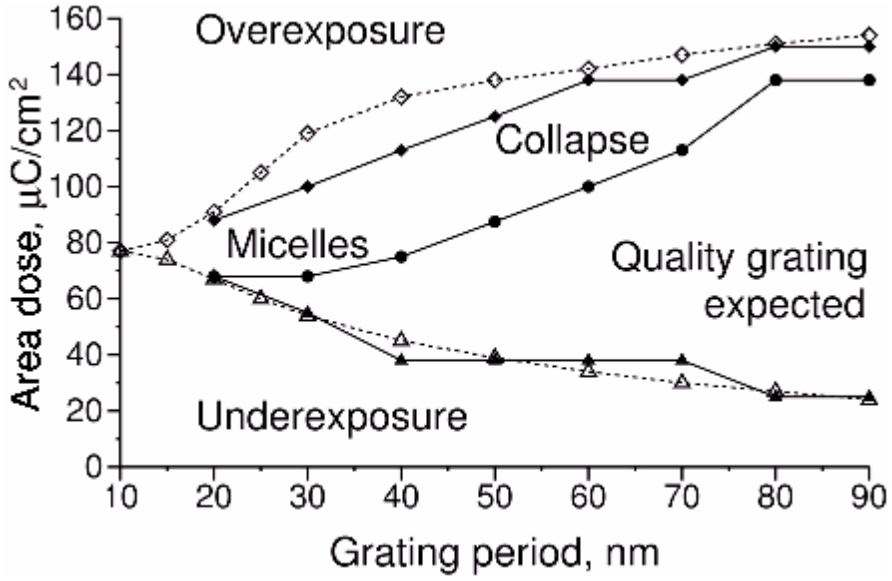

Figure 5: Plot of the characteristic morphologies in PMMA for various grating periods and area exposure doses using 10 keV voltage. Filled symbols show experimental results for the conditions as in Fig.1: triangles denote the boundary for underexposure (insufficient clearance); diamonds denote the boundary for overexposure (excessive clearance), and circles indicate the boundary for collapse or miscellization. Open symbols show the results of numerical modeling of clearance. [11, 9, 30]

2.5 **Electron Beam Modeling and Simulation**

Because of the complexity of the EBL process, it is advantageous to employ simulations to better understand the complex interplay of parameters and aid in optimization.

The process of laboratory EBL experimentation is expensive, time-consuming, and involves numerous interrelated conditions such as exposure energy and dose, time and temperature of development, etc. Hence, implementing the process in an EBL simulator provides an immense value and saves lot of time. The objective of computer simulation of the processes of electron beam lithography is the prediction of the outcome after exposure and development. Research on modeling and simulation of EBL in order to further understand and optimize the process spans more than four decades. [12, 51, 52, 53, 54, 55] Extensive modeling studies of the processes of electron penetration, scattering and energy deposition in resist and substrate materials have been covered by Monte-Carlo [56, 57, 58, 59, 60, 61] simulations and the kinetic transport theory.

The accurate prediction of the simulated resist profiles strongly depend on the models adopted for the physical processes of inelastic interaction of electrons with the exposed resist and accurate representation of the process of development.[12, 56] Various software exist for EBL modeling and they include CASINO, Raith with proximity correction, and several other simulators, which are mentioned in section 2.5.3.

2.5.1 **Monte Carlo Modeling**

The Monte Carlo method is used for studying electron beam-surface interaction, including forward scattering electrons, backscattering electrons and secondary radiation products as a function of the beam and material parameters. [62] The method is based on applying random sampling techniques and predicting the average behavior of a large number of electrons from the study of a representative number of events. [51] When an electron impacts a surface, it would be scattered elastically or inelastically. Elastic scattering occurs when the electron experiences a change in direction but does not transfer its energy beyond ballistic scattering. On the other hand, inelastic scattering occurs in collisions when a part of energy is spent in ionization or other changes in chemical structure of the material.

The Monte Carlo method can be used to simulate and predict the outcome of elastic and inelastic collisions as determined by the total cross section of electron scattering [51]. The probability that an electron is either elastically or inelastically scattered is implemented by using randomly generated numbers and defining a threshold which represent either case of scattering such that the number (RND) lies between 0 and 1 [51]. Since any number in the interval has an equal chance of being selected, applying this random selection scheme a large number of times effectively predicts the expected probability.

In order to simulate an electron trajectory using the Monte Carlo method, the effects of elastic and inelastic scattering are calculated from appropriate theoretical models [51, 62] or obtained experimentally [51] to determine scattering angles, average distance between scattering sites (mean free path)and the rate of

energy loss during various events. From these parameters and using the equations of analytical geometry relating scattering angles and step length to successive electron locations, the electron trajectory can be simulated from its entry location to final thermalization. [62] By simulating a large number of trajectories, a statistically accurate representation of possible scattering events [51] can be obtained.

2.5.2 **CASINO**

Literature describing the electron scattering simulation tool CASINO is listed in a web page. [63] CASINO, an acronym, from "monte CArlo SImulation of electroN trajectory in sOlids", is a Monte Carlo simulation of electron trajectory in solid specially designed for the beam interaction with bulk and thin foil materials. The single scattering Monte Carlo process is complex and the program is specifically designed for low energy beam interaction and can be used to predict many of the measurable signals such as x-rays and backscattered electrons, generated for example in a scanning electron microscope. The program can be used for the accelerated voltage range from 0.1 keV to 30 keV.

CASINO is designed to simulate a large amount of electron trajectories in solids such as Si or other materials. It also has the capacity to handle multi-layer samples and grain boundary geometry. The main idea is to simulate enough electron trajectories to represent the condition used to image structures in a scanning electron microscope (SEM). Thus, it is possible to predict numerically the signals observed in the SEM.

2.5.3 **Other electron beam simulators**

There are other electron beam simulation tools developed for use and some of these include: EGSnrc which is a Monte-Carlo simulator for coupled electron-photon transport with an energy range of 1 keV to 10 keV [64]; CHARIOT which uses the Monte Carlo method simulator to understand and predict electron-solids interaction including image formation in SEM, electron energy deposition, backscattering coefficients, emission properties, and transmission of electrons through thin films [65]; NISTMonte, which is a Monte Carlo simulator of electron and x-ray transport in solid materials, [66] recently replaced with NIST DTSA-II. [67] WinXRay, a Monte Carlo simulator for electron trajectory in solids, extends the capabilities of CASINO to include statistical distributions for backscattered electrons, trapped electrons and energy loss curves for x-ray. [68]

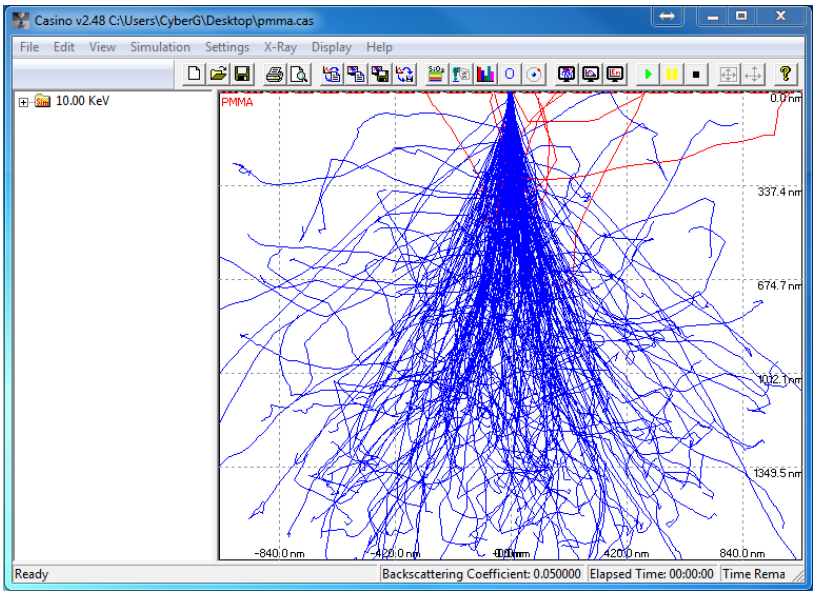

Figure 6: Example of CASINO[63].Simulation of electron trajectories in PMMA at using 200 electrons at 10 keV. PMMA thickness is 55 nm.

PENELOPE, another Monte Carlo package performs simulation of coupled electron-photon transport in arbitrary materials and complex quadric geometries [69]. Furthermore David Joy's Monte Carlo simulators account for single and plural scattering in thin foils and bulk samples; [70] Electron Flight Simulator is a software tool which allows for modeling sample chemistry and can also give detailed views of electron beam – sample penetration, and x-ray generation under different microscope conditions; [71] and MCSet, simulator allows generating electron trajectories for SEM applications. [72]

2.5.4 **NINT's Electron Beam Lithography Simulator**

The e-beam simulator developed recently by NINT and U of A [12, 73, 74] describes both exposure and resist dissolution, and provides tools for visualization, analysis and optimization of electron-beam nanolithography. [12] The simulator uses an analytic kinetic approach to electron transport to predict three dimensional polymer scission distributions for arbitrary patterns and a full kinetic treatment of the dissolution process.

The tool has capabilities to accept the following input parameters: thickness of resist (presently PMMA), substrate material data, high-resolution writing pattern (single features or periodic), electron energy (1 - 50 keV), electron dose, time and temperature of development. It can output 3D distributions of the resist chain scission probability, 3D distributions of the fragments, 3D clearance profiles, 2D cross sectional profiles and 1D line plots.

The simulator can be used to predict the exposure dose at which clearance of the resist is achieved, for a given set of exposure and development conditions. The simulator can also be useful to calculate the levels of exposure (the yield of main chain scission) for given exposure dose. Figure 7 shows screenshots of the capabilities of the software implemented currently. Further upgrades are in progress.

2.5.5 **Model of Exposure and Fragmentation of PMMA**

The details of the NINT simulator model implementation are discussed in literature. [12, 30, 13]

The model of exposure adopted in the simulator employs the kinetic transport theory to determine the distribution of primary, secondary, and backscattered electrons. The inelastic interactions of electrons of energy *E* with resist atoms are described with the differential cross-section,

$$\mu(E,\varepsilon) = \sum_i N_i c_i \sigma(E,\varepsilon,U_i), \qquad (1)$$

where ε is the relative energy transfer, $\varepsilon = \Delta E/E$, $\sigma(E,\varepsilon,U_i)$ is the Gryzinski differential inelastic cross-section, N_i is the number density of shell electrons with the binding energy U_i, and c_i is an energy-dependent weight factor. [13]

The first step is the computation of the spatial distribution of scission events in a planar layer of PMMA exposed to a point beam of primary electrons. The number of inelastic collisions of secondary, tertiary, and higher electrons, produced by a

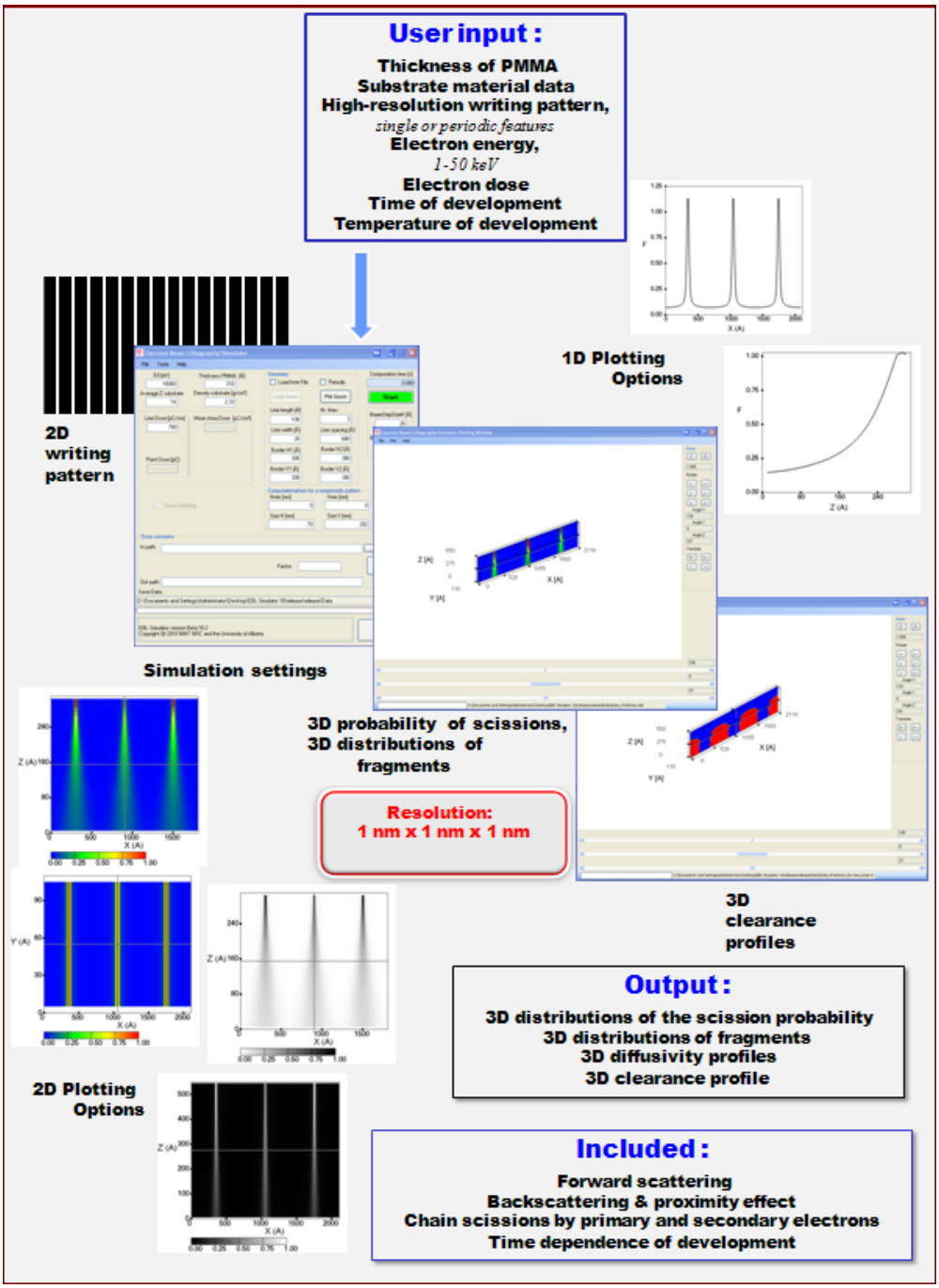

Figure 7: Features of EBL Simulator. (Adapted from previous works [12, 75])

beam of primary electrons with energy E_P moving along a given direction, is available from a pre-computed table, which has been generated by solving the Boltzmann transport equation for the electrons. [13] Iterative numerical solution of the Boltzmann equation produces a distribution function of secondary electrons moving with energy E at a distance ρ from the primary beam, $f_S(E_p, \rho, E)$. The total exposure profile $f(E_p, \rho, E)$ is the sum of the exposure profiles caused by both primary (P) and the secondary (S) electrons and is given by the distribution function,

$$f(E_p, \rho, E) = f_p \delta(\rho)\delta(E - E_P) + f_S(E_p, \rho, E), \quad (2)$$

where f_p is a flux constant, and δ is the Dirac delta function. Eqn. (2) is then employed to compute the corresponding rate of scissions of the C-C bonds in the main chain in PMMA,

$$Y(E_p, \rho) = \int f(E_P, \rho, E) v \, \mu_{c\text{-}c}^{tot}(E) dE, \quad (3)$$

where v is the electron velocity and $\mu_{c\text{-}c}^{tot}$ is the total cross-section of inelastic collisions with valence electrons involved in backbone C-C bonds in PMMA. [13] In the simulator, the radial distribution of the rate of scission, $Y(E_p, \rho)$, is converted into the corresponding average number of scissions per monomer, per electron, denoted as the yield of scissions, $w(E_p, \rho)$.When this quantity is less than unity, it can also be interpreted as the probability of the main chain scission.

Broadening of the primary electron beam is described through the classic diffusion approximation. [52, 53, 76, 77] For a point source of primary electrons traveling through a depth *z*, the lateral broadening is given by

$$P_P(\rho,z)\rho d\rho = \frac{3\lambda}{(z_{\max}-z)^3}\exp\left(-\frac{3\lambda\rho^2}{2(z_{\max}-z)^3}\right)\rho d\rho\,, \qquad (4)$$

Where *z* is depth (*z*=0 corresponds to the bottom of the resist interfacing the substrate), z_{max} is the thickness of the resist, $z_{max} - z$ is the distance from resist surface, and λ is the depth dependent elastic transport mean free path. The convolution $P_P(\rho,z)$ * $w(E_p,\rho)$ produces the depth dependent radial distribution of the yield of scissions in a planar layer of PMMA exposed to the point electron beam, $w_P(\rho,z)$.

Finally, scissions by backscattered electrons from the substrate are accounted for. The backscattering coefficient and the distribution of backscattered electrons over the emission energy are computed employing the Staub distribution. [78] For the distribution of backscattered electrons over the emission angle θ, the dependence cos(θ) is used based on reasonable agreement with numerical and experimental results reported in literature. [54, 79] The spread of the emission points is given by the distribution,

$$P_B(\rho)\rho d\rho = \frac{2}{\sigma^2}\exp\left(-\frac{\rho^2}{\sigma^2}\right)\rho d\rho\,, \qquad (5)$$

where ρ is the distance relative to the impact point of the primary electron, and

$\sigma(\text{nm}) = 4.52 \cdot 10^3 r^{-1} \left(E_{Ps} / 2 \cdot 10^4 \right)^{1.65}$, where r is density of the substrate in g/cm^3 and E_{Ps} is the energy of primary electrons (in eV) when they reach the substrate. The convolution of the function $P_B(\rho)$ and the distribution of primary electrons at the bottom of the resist, $P_P(\rho,0)$ describes the emission of backscattered electrons. The propagation of backscattered electrons, generation of the corresponding secondary electrons, and the chain scissions in the resist, produce a depth-dependent radial distribution of the yield of main-chain scissions by backscattered electrons, $w_B(\rho,z)$.

By adding together the local yields of scissions generated by forward and backscattered electrons, $w_P(\rho,z)$ and $w_B(\rho,z)$, the total depth dependent radial distribution of the scissions of the main chain in a planar layer of PMMA exposed by a point beam, $w(\rho,z) = w_P(\rho,z) + w_B(\rho,z)$ is obtained.

In the final step, a convolution of the radial distribution of the yield of scissions from a point beam $w(\rho,z)$ with the writing pattern in the lateral plane {x, y}, results in a 3D spatial distribution of the yield of scission per PMMA monomer, $W(x,y,z)$. Figure 8 outlines the model of exposure adopted in the simulator. In the model, the yield of main-chain scissions is computed directly through the differential cross-section for inelastic collisions resulting in the scissions. [13] The model avoids uncertainties related with the conversion of the distributions of deposited energy into the number of main-chain scissions through the empirical radiation chemical yield.

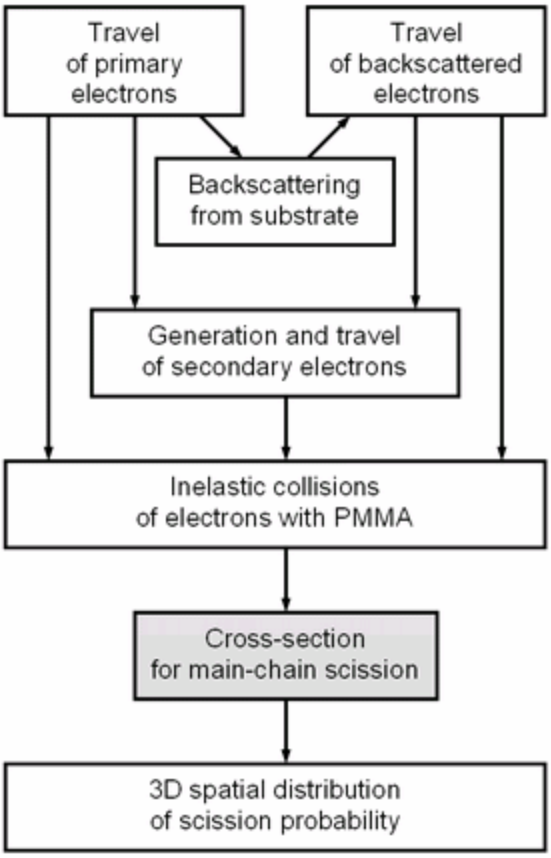

Figure 8: Sketch of the model of exposure in EBL Simulator [9]

2.5.6 **Model of Development**

After computing the 3D distributions of the yield of scission in the resist as described in the section 2.5.5, the local probability of scission is converted into the local volume fractions of PMMA fragments of various size $\varphi_n(x, y, z)$, where n is the number of monomers in a fragment.

The probability of bond scissions rather than the average number of scissions per bond is required and for this reason, the distribution $W(x, y, z)$ has been truncated at the level of 1 at locations where higher average numbers of scission per bond

have occurred, so that $W(x,y,z) \leq 1$. The truncated value W is referred to as the probability of scissions.

Assuming that the probability of bond scission does not depend on bond position in the PMMA chain or its length, the distribution of polymer chain length after the scission process can be found, which depends on $W(x,y,z)$ and the initial number of monomers in a resist molecule, n_{init}. At the condition $n_{init}\, W \gg 1$, which is satisfied for n_{init} = 9600, the geometrical distribution is applicable. [80, 81] The corresponding probability to find a fragment containing n monomers at a given location $\{x,y,z\}$ is expressed by

$$C_n(x,y,z) = W(x,y,z)\big(1 - W(x,y,z)\big)^{n-1}, \tag{6}$$

and the volume fraction of fragments containing n monomers is found to be

$$\varphi_n(x,y,z) = \frac{n\,C_n(x,y,z)}{\sum_{n=1}^{\infty} n\,C_n(x,y,z)} = nW^2(x,y,z)\big(1-W(x,y,z)\big)^{n-1}. \tag{7}$$

For this purpose, the kinetic process of clearance is described by the movement of the resist–developer interface, which depends on the local distribution of fragments size $\varphi_n(x, y, z)$. The rate of dissolution is defined by v = dL/dt, where L is the depth of shrinking of the resist.

The kinetics of resist shrinking is described by:

$$\frac{dL}{dt} = \eta D L^{-1}, \tag{8}$$

where D(x, y, z) is the local diffusivity of PMMA fragments and η is a constant

coefficient that depends on the interaction of developer with PMMA. In the case of constant diffusivity D, Eqn. (8) predicts the dependence $v \sim (D/t)^{1/2}$, where t is time of development. The approximate model of resist shrinking described by Eqn. (8) implies that at the nanoscale, the rate of resist dissolution is a function of the entire history of the process of development, and thus depends on time explicitly.

For the diffusivity of PMMA fragments of size n, the proportionality $D_n \sim n^{-\alpha} \exp(-U/kT)$ is employed where U is the activation energy and the factor $n^{-\alpha}$ describes the mobility of fragments of size n in a medium whose properties are represented by power α. In most polymers, α varies from 1 in dilute solutions of small molecules to 2 for denser melts of longer polymer chains. [80, 81] In exposed PMMA, an effective location-dependent diffusivity can be introduced, $D'(x, y, z) = \langle \eta D_n \rangle = \langle \beta n^{-\alpha} \rangle$, where $\alpha = 1 + \langle n \rangle / \gamma$ for average fragment size $\langle n \rangle$ less than γ and α = 2 otherwise. [9, 12]

The development process is modelled by an efficient finite-element numeric algorithm. A sequence of discrete dissolution steps, where time δt required to dissolve a resist layer of thickness δL, is determined by $\delta t = 2L\delta L / D'(x, y, z)$. The simulation provides the location of the 3D resist-developer interface as a function of time, with a 1 nm spatial resolution. The model parameters β and γ may depend on temperature but not on other process conditions, and have been evaluated by fitting the computed percentages of PMMA left on the substrate to the corresponding experimental results obtained from SEM cross-sectional profiles

for gratings. [12, 30]

3 Experimental Setup and Methodology

3.1 Description of Equipment

The instruments used during the experimental research include the following:

3.1.1 Raith 150/150^{TWO} EBL System

Ultra high resolution, low voltage (0.1 – 30 keV) EBL tools used to write patterns on the wafer. Both systems were used for exposure at different times in my experimental sessions.

Figure 9: The Raith 150 and Raith 150^{TWO}EBL Systems

3.1.2 Hitachi S-4800 Field Emission SEM

Ultra high-resolution scanning electron microscope for imaging the sample surface by scanning it with a beam of electrons in a raster scan pattern.

3.1.3 Headway Spinner/Hotplate

The Headway spinner is a manual resist dispense system with interchangeable bowls, allowing multi-purpose processing. The hotplate is used for baking the

sample to drive-off residual solvent.

Figure 10: Hitachi S-4800 Field Emission SEM

Figure 11: Headway Spinner/Hotplate

3.1.4 **VASE Ellipsometer:**

Variable Angle Spectroscopic Ellipsometer is used for high accuracy measurement of film thickness and to determine the various optical properties of thin films.

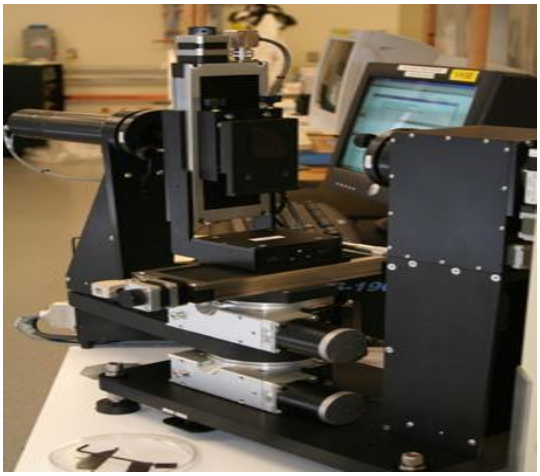

Figure 12: VASE Ellipsometer

3.1.5 **Gatan Sputtering System**

This instrument is used to deposit metal films on thin films to serve as anti-charging layer.

Figure 13: Gatan Sputtering System

3.1.6 **Filmetrics Resist and Dielectric Thickness Mapping System**

This instrument is used for optical (non-contact and non-destructive) measurement of the thickness of thin films.

Figure 14: Filmetrics Resist and Dielectric Thickness Mapping System

3.1.7 **Stir Kool Cold Plate**

This instrument is used to cool the developer and stopper to -15º C while the magnetic stirrers placed in the beakers are used to eliminate temperature gradient in the solvents.

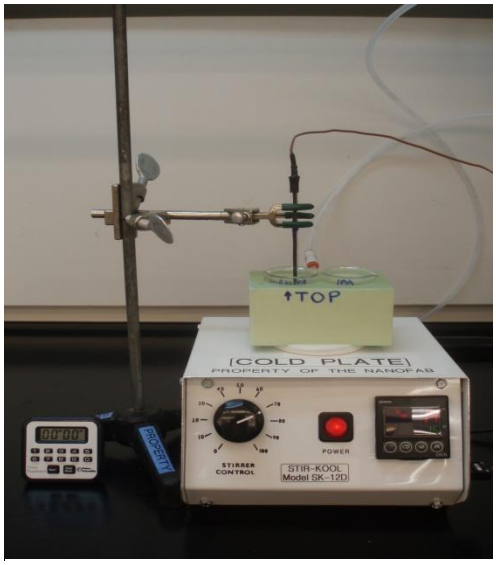

Figure 15: Stir Kool Cold Plate Setup

3.2 **Sample Preparation**

Silicon wafers diced to 1.5 cm x 1.5 cm were cleaned in Piranha (75%

sulphuric acid and 25% hydrogen peroxide) for 15 minutes to remove organic residues from the substrates. The wafers are rinsed in the dump-rinser in a 5-cycle rinse process. Then, the wafers are blown dry and pre-baked for 5 minutes on a hotplate to drive-off residual water and dry the samples.

Thereafter, the wafers were spin coated with 950 K PMMA to form a film of 30 nm – 47 nm in thickness using a Headway Spinner and soft-baked on a hotplate at 175° C for 5 minutes after which they were allowed to stand for several minutes to cool down. The thickness of the resist coating was measured using the VASE Ellipsometer or Filmetrics Resist and Dielectric Thickness Mapping System.

3.3 **Exposure**

The wafer to be exposed to a beam of electrons was loaded into the sample chamber of the Raith 150/150^{TWO} EBL system. Thereafter, several iterative steps to optimize the working distance (focus), align the aperture and correct astigmatism in the electronic lenses were carried out to obtain a good exposure. The typical exposure parameters used for 1 keV and 2 keV exposures are given in Table 1.

The next step was to make electron beam exposure using the Raith 150/Raith 150^{TWO} e-beam lithography system using patterns created using the Raith 150 GDS II software. Several patterns were exposed during the experimental and are depicted in Figure 16 and Figure 17.

Table 1: Typical settings for Raith 150/150^{TWO} EBL system

ExposureParameter		**Raith 150**	**Raith 150^{TWO}**	**Raith 150^{TWO}**
		1 keV	**1 keV**	**2 keV**
Aperture size (µm)		7.5	7.5	7.5
Beam Current (pA)		5.7	9.7	9.7
Aperture Alignment	**X (%)**	2.7	-1.527	0.654
	Y (%)	15.3	-16.142	-9.393
Stigmation	**X (%)**	3.2	-25.480	-6.615
	Y (%)	-10	-12.340	-11.224
Working Distance	**mm**	6.929023	6.99012	8.04597
Z	**mm**	19	21	20

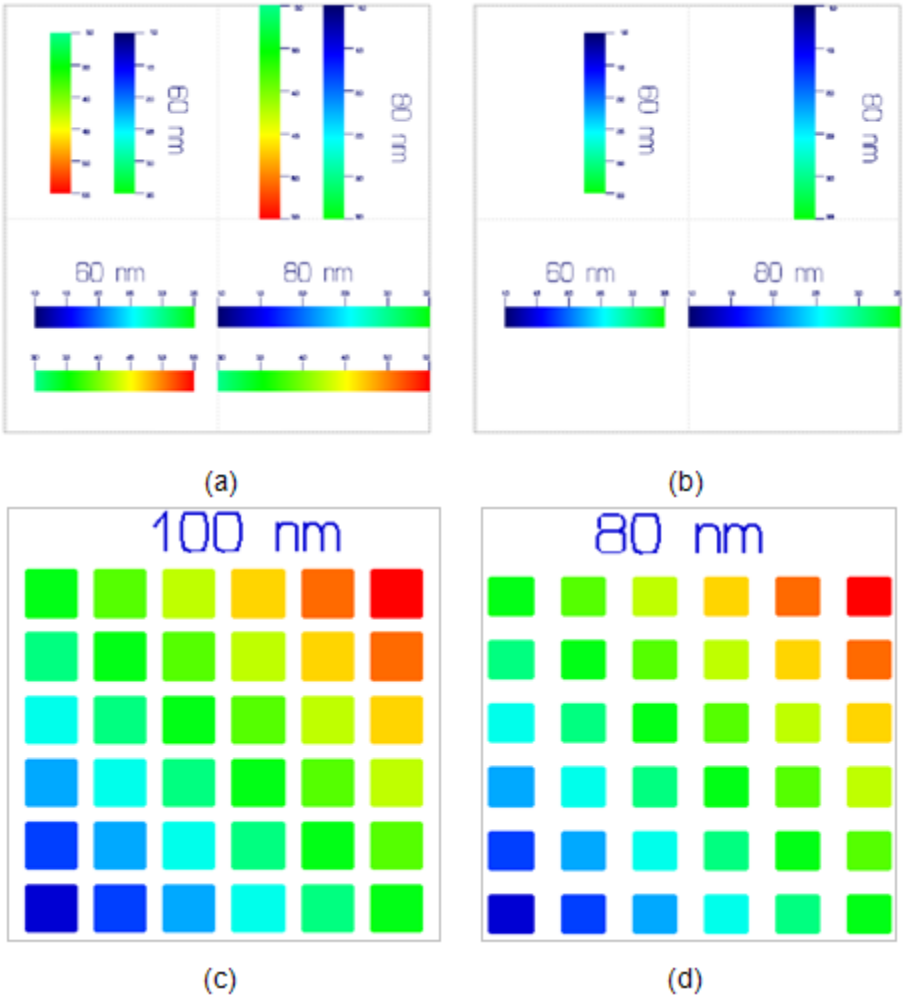

Figure 16: Examples of initial exposure patterns created with Raith GDS II software: (a) 60 nm and 80 nm pitch gratings with a dose gradient (1.0 - 5.5) in horizontally stacked and vertically stacked directions; (b) 60 nm and 80 nm pitch gratings with a dose gradient (1.0 - 3.5) in horizontally stacked and vertically stacked directions; (c) 100 nm pitch array of dots and (d) 80 nm pitch array of dots. Each line in the grating has 0.2% higher exposure than the line to its left. The color shading of the gratings and arrays of dots indicates increasing dose from blue (minimum) to red (maximum).

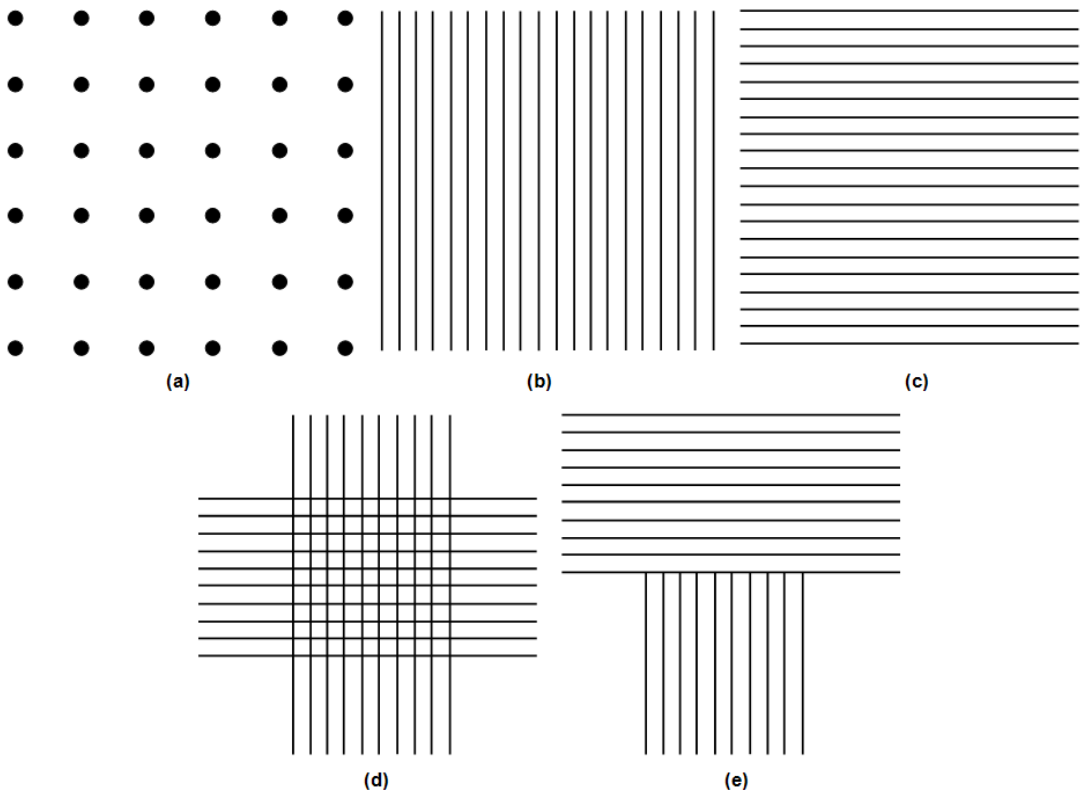

Figure 17: Examples of initial exposure patterns created with Raith GDS II software: (a) array of single-pixel dots (shown in detail) (b) horizontally stacked single pixel periodic grating pattern; (c) vertically stacked single pixel periodic grating pattern; (d) array of single pixel lines in a cross configuration; (e) array of single pixel lines forming a T-junction. For dot array design (a), initial pitches of 80 nm and 100 nm were used, whereas designs (b-e) employed an initial line pitch of 100 nm[1].

Figure 16 (a) shows GDS II patterns of 60nm and 80 nm dose test gratings composed of arrays of lines in horizontally stacked and vertically stacked directions with dose factors varying from 1.0 to 5.5. Dose test gratings are lines with a geometrically increasing dose factor that helps to experimentally determine the optimum exposure and development process parameters where good quality

[1]*A version of this figure has been published. J. Vac. Sci. Technol. B 29, 06F312 (2011); doi:10.1116/1.3657512.*

patterns can be fabricated. [82] Dose test gratings are used to determine the applicable dose window for given exposure and development conditions and are applied to characterize the repeatability of the particular experiment process as well as test the working conditions of the Raith 150/150^{TWO} system. [82] Dose factors give information about the quantity of charge applied per unit length (or per dot for dot arrays) for each line (or dot) in the grating (or dot) pattern. By setting the proper line (point) dose range, information about the optimum dose values for a grating (dot) array with a given pitch and developed at fixed development conditions can be obtained in one experiment. [82] Figure 16 (b) shows GDS II patterns of 60 nm and 80 nm arrays of lines in vertically stacked and horizontally stacked directions with dose factors of 1.0 - 3.5. The dose factors increase from the lowest dose shown in blue to the highest dose shown in red. Each dose test grating is composed of 10 μm long lines spaced according to the grating period. The dose increment between two neighboring lines is 0.2% in order to generate locally constant dose condition. The design incorporated both vertically stacked and horizontally stacked lines in order to isolate the effects of grating orientation on the morphology of the gratings fabricated. Horizontally stacked lines refer to gratings arranged vertically with a specific pitch and the dose factors increase from left to right (horizontally). Vertically stacked lines refer to gratings arranged horizontally with a specific pitch and the dose factors increase from top to bottom (vertically). Figure 16 (c) shows GDS II patterns of 100 nm pitch array of dots with increasing doses varying from 1 to 11 while

Figure 16 (d) shows GDS II patterns of 80 nm pitch array of dots with increasing doses varying from 1 to 11.

Figure 17 shows other isolated standard test structures such as (a) zoomed in dots, zoomed in isolated (b) vertical and (c) horizontal lines, (d) crossed lines and (e) T-junctions. These demonstrate different exposure behavior than dense gratings due to different proximity effects.

Generally, all the patterns were placed at the approximate center of the write field to reduce the beam current fluctuations as it approaches the edge of the write field or starts to write in a new field. The write field is a pre-defined (square) area sub-unit of the exposure grid in the input writing pattern. In order to complete multiple exposures at the same time, up to 4 exposures are done on each sample. The sample is then cleaved into smaller samples of approximately 0.75 cm by 0.75 cm.

3.4 **Development**

After exposure, the wafers were developed at a cold temperature of -15 °C (-20 °C for density multiplication of 100 nm gratings) in MIBK:IPA 1:3 mixture followed by a rinse in IPA, acting as a stopper. The development times were 5, 10, 15 and 20 sec in the cold solvents using the setup of the Stir Kool Cold Plate as shown in Figure 15. The stopper bath temperature was the same as that of the developer.

3.5 **Characterization**

Approximately 5 nm of Cr was deposited on the developed sample as an anti-

charging layer using the Gatan sputtering system before surface imaging in a Hitachi S-4800 field emission SEM at NINT.

3.6 **EBL Simulator Development and Testing**

The EBL simulator [12, 73 , 74] introduced in the section 2.5.4 was used in carrying out modeling and simulation of experimental conditions before laboratory experimentation. The simulator was developed using Microsoft Visual Studio (Professional) 2005 using the OpenGL [83] application program interface for plotting. It is tested and runs under Windows XP and Windows 7. My contribution to the development of the simulator was the development of the 2D plotting capabilities, minor improvement to 3D plotting and the graphical user interface, as well as writing a part of the documentation. [73] A comprehensive publication detailing the capabilities of the simulator is available in previous publication. [12]

Figure 18 (a) shows the main window of the EBL application interface. This interface provides the main entry point to running exposure and development simulations and several parameters can be entered or selected such as the energy, resist thickness, choice of periodic or non-periodic patterns or even complex graphic images in TIFF [84] format, point, line or area dose, the number of lines to be simulated, pitch, spacing, and so on. A typical simulation can be run by following steps 1 – 7 highlighted in the main simulator interface shown in Figure 18 (a). The simulation begins when the start button is pressed after which it computes the 3D probability of scission at every point in the resist for the input pattern and the subsequent development profile. The simulator accounts for

forward and backscattering of electrons, proximity effects, chain scission by primary and secondary electrons, and time and temperature dependence of development. In addition, the simulator outputs the 3D distribution of the probability of scission, distribution of fragments, diffusivity profiles and clearance profiles. Additional plotting capabilities include visualization of the 2D cross sectional profiles and 1D line plots in X, Y and Z directions. Some of the outputs of the simulator are shown in Figure 18 (b-d). Figure 18 (b) shows the 2D (XZ) cross section of a yield of scission while Figure 18 (c) shows the same plot but in grayscale. Figure 18 (d) shows the Z dependence (1D) of the yield of scission in an exposed spot.

In order to run a simulation, the simulator program is launched from its installed location and the main program interface as shown in Figure 18 (a) is presented to the user. This example illustrates a case of low voltage exposure simulation, which was used as part of this thesis. The parameters required for exposure simulation are: 1000 eV (1 keV) for the exposure energy, 310 Å for PMMA thickness, and a line dose of 80 pC/cm and the "Periodic" checkbox is checked to simulate periodic grating. The number of lines and their length can be specified or a defaults value used. The default values of 3 for number of lines and 100 nm for length were used in this case. Next, the pitch was specified by entering the line width (20 Å) and line spacing, (580 Å) for a pitch setting of 60 nm. The software is capable of visualizing the input pattern before simulation which can be activated by clicking the “Plot Geom” button which displays the pattern shown as

an inset in Figure 18 (a). To start the simulation, click the "Start" button, which generates the probability of scission data file.

Thereafter, the probability of scission can be visualized by using the plotting tools in the simulator to generate a 1D, 2D and 3D plot of the data file. The scale bar shown in Figure 18 (b) gives the normalized scission probability and this is used to interpret the 2D plot of Figure 18 (b). The red regions of the plot are areas in which there is a higher scission probability while it is lowest in the blue areas. In order to predict if clearance can be obtained at a particular set of exposure conditions, a 1D Z-plot dependency in the core of the spot is output showing the actual levels of the yield of scission at different heights, F-value, in the resist. If this F-value at the bottom of the resist is of the order of 1 or greater, then clearance can be achieved at this exposure condition. A general idea of whether or not clearance can also be obtained by simply observing the 2D XZ plot as shown in Figure 18 (b). If the scission areas of the resist close to the bottom is blue (meaning a low yield of scission), it is less likely that clearance will not be achieved experimentally under these exposure conditions.

Furthermore, clearance profiles can also be simulated directirly for exposure pattern, and duration and temperature of development. Figure 18 (e, f) show examples of clearance profiles in PMMA exposed by 1 keV electrons at different doses. In Figure 18 (e), the resist is not cleared down to the substrate at a dose of 50 pC/cm while at a higher dose of 100 pC/cm and shown in Figure 18 (f), there is total clearance of the resist down to the substrate.

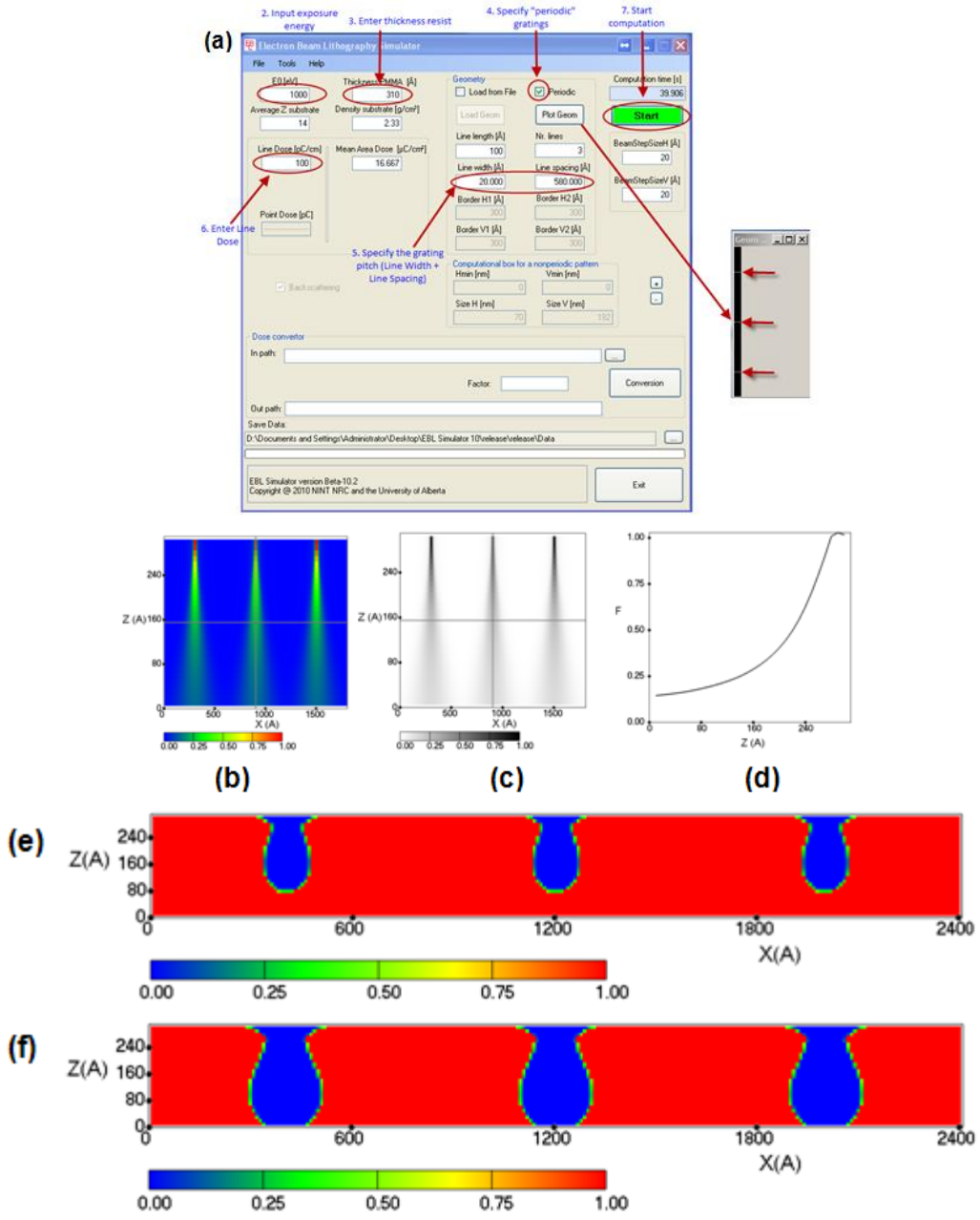

Figure 18: EBL Simulator with sample screen shots showing some of its capabilities, (a) The main window of the EBL Simulator; (b) 2D Plot of XZ cross section of probability of scission of 2 dots - in color; (c) 2D Plot of XZ cross section of probability of scission of 2 dots - in grayscale; and (d) 1D Plot of the probability of scission showing the depth dependence in an exposed spot, 2D X-Z clearance profiles in gratings at two different doses at 1 keV (e) Under-exposed at a dose of 50 pC/cm (f) Well Exposed at a dose of 100 pC/cm.

The shape of the development profile does not always necessarily follow the symmetry of the distribution of exposure. For example, in Figures 18 (e) and (f), there is corner rounding during the development and this is due to the fact that development progresses from both the top and side of the features leading to corner rounding. Therefore, modelling of exposure is not always sufficient because the process of development can alter the geometry. It is therefore mandatory to run the exposure and development processes of the simulation to obtain accurate results.

In order to pre-determine the initial experimental conditions, the simulator was run as described earlier in this section. The developed profiles were output for comparison as shown in Figure 18 (e) and (f) and a dose where the developed profile approaches clearance or is almost cleared was selected as initial conditions. This is because using in order to capture the entire dose window under a set of experimental conditions, it is important to be able to see clearly regions of under-exposure, good exposure and over-exposure. In the simulation using 60 nm pitch gratings exposed at 1 kV and developed for 5 secs at -15 ºC, under-exposure was observed using a line dose of 80 pC/cm while clearance was predicted at 100 pC/cm and higher doses.This was ideal to write patterns using a dose range varying from 1.0 to 5.5 which translates to an actual dose window of 80 pC/cm to 440 pC/cm.

4 Results and Discussion

4.1 Introduction

In this section, selected results for dots and gratings patterns fabricated using ultra-low energy exposures of 1keV and 2 keV and developed at cold temperatures are presented. Experimental results of density multiplication and comparison with modeling of exposure for similar conditions are discussed.

In the process of experimentation, the performance of the Raith 150/150^{TWO} EBL system has been tested in the ultra-low energy regimes of operation. The stability of the machine had not previously been explored in this regime. The results of these tests are also discussed, challenges identified and possible solutions suggested. In describing the electron dose for gratings, the line dose notation is used, whereas the point dose is used for describing exposure of dots.

4.2 The Applicable dose windows for fabrication of nanostructures

Nanofabrication of structures at low voltages, 1 keV especially, proved to be one of the most challenging processes for EBL. [30, 22, 41]

This is largely due to limited resolution as a result of strong forward scattering of the electrons, proximity effect, and a reduced dose window. This section will address experimental results focusing on the quality of the grating morphology, its representation by the dose windows and comparison of the pattern quality for all experiments. In the end, the optimum conditions for lithography at low voltages of 1 keV and 2 keV using the Raith 150/Raith 150^{TWO} will be identified.

In the described experiments, high-density 60 nm and 80 nm pitch periodic gratings were fabricated in a 31 nm thick PMMA layer on Si (100) wafers using 1 keV electrons with the input pattern shown in Figure 16 (a).

The first run was the basic experiment to get an idea of the results that could be obtained at 1 keV exposures. The goal was to determine the applicable doses and other processing conditions at which gratings could be fabricated and thereafter improve the results by optimizing the processing conditions. The initial conditions were chosen using the simulator predictions as described in section 3.6. Using the dose test patterns shown in Figure 16 (a), the starting line dose was chosen to be 80 pC/cm with the dose factor varying from1.0 to 5.5, yielding a dose range of 80 pC/cm – 440 p/cm. After exposure, the samples were developed for 5 sec, 10 sec, 15 sec and 20 sec in a MIBK:IPA 1:3 mixture at -15°C. Figure 19 (a-d) shows representative low magnification SEM micrographs of the patterns generated on the resist. The micrographs were taken from a single sample developed for 5 sec. As seen from the micrographs, dose windows exist for which grating patterns can be fabricated. However, the quality of the gratings varies on different chip areas. Generally, three regimes exist for which there is a marked difference in the morphology of gratings: under exposure, good exposure and over exposure. [30, 32, 82]

Under exposure of PMMA occurs when the electron dose is insufficient to cause enough chain scissioning in the polymer to achieve clearance of the resist in exposed areas. As a result, the exposed areas of the resist are not cleared down to the substrate. Under exposure can also be seen in Figure 20 showing horizontally

stacked and vertically stacked gratings, respectively. Figure 20 (a) shows under exposed gratings fabricated with a line dose of 200 pC/cm while Figure 20(b) shows under exposed gratings fabricated with a line dose of 160 pC/cm with both characterized by low contrast in exposed areas compared to unexposed areas. Figure 21 shows well exposed gratings with high contrast in exposed areas compared to unexposed areas. The grating patterns are well defined with low line edge roughness. Figure 21 (a) shows 60 nm pitch horizontally stacked gratings patterned with a line dose of 320 pC/cm while Figure 21 (b) shows 60 nm pitch vertically stacked gratings fabricated with a line dose of 280 pC/cm.

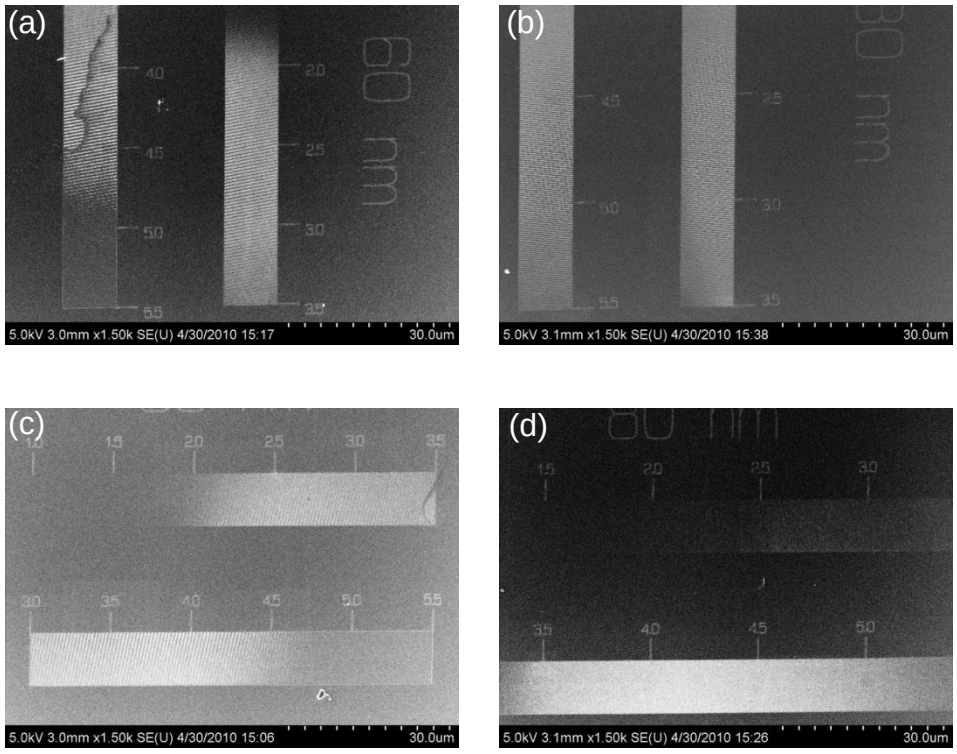

Figure 19: Low magnification SEM micrographs of (a) 60 nm vertically stacked dose test gratings; (b) 80 nm dose test gratings; (c) 60 nm horizontally stacked dose test gratings; and (d) 80 nm horizontally stacked dose test gratings.

Figure 22 shows over exposed gratings with collapsed or missing features. Figure 22(a) shows 60 nm pitch horizontally stacked gratings patterned with a line dose of 360 pC/cm while Figure 22(b) shows 60 nm pitch vertically stacked gratings patterned with a line dose of 320 pC/cm. The strong forward scattering of the electrons in the resist at low voltages creates large undercut profiles in the PMMA walls and at high exposure dose, more PMMA is removed from the exposed areas. This ultimately causes the base of PMMA walls to be weakened and leads to collapse during development. [9, 30]

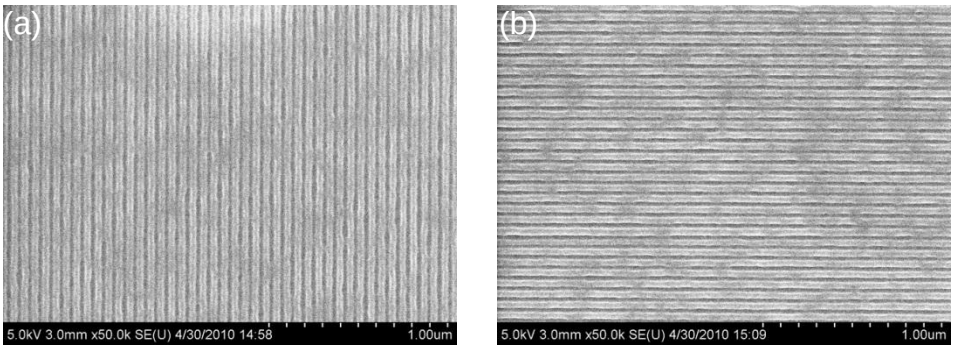

Figure 20: Example of underexposure in (a) 60 nm horizontally stacked dose test gratings and (b) 60 nm vertically stacked dose test gratings

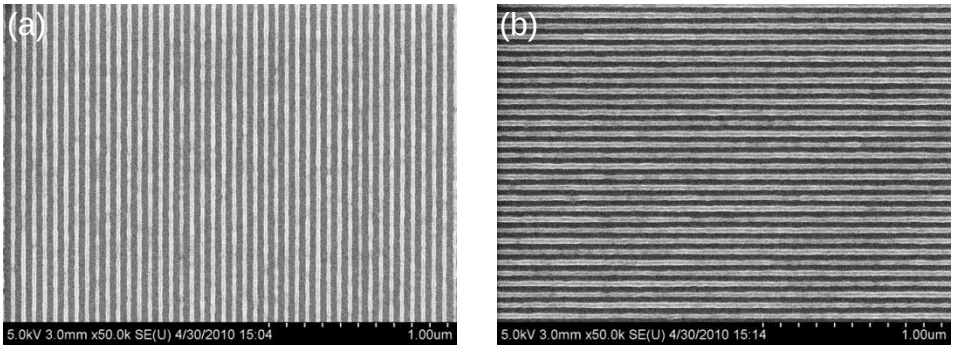

Figure 21: Example of good exposure in (a) 60 nm horizontally stacked dose test gratings and (b) 60 nm vertically stackeddose test gratings

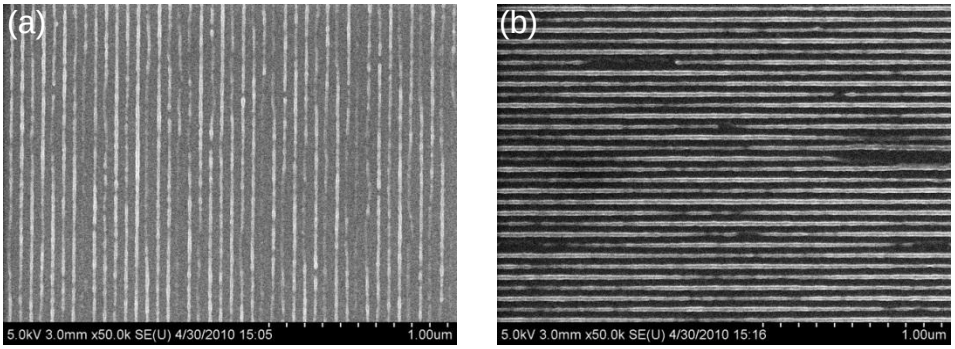

Figure 22: Example of over exposure in (a) 60 nm horizontally stacked dose test gratings and (b) 60 nm vertically stacked dose test gratings

The dose window gives an indication of the applicable doses for which a qualitygrating pattern can be generated. This knowledge, along with other process conditions, is critical in EBL in order to reliably generate quality patterns. Figure 23 shows example dose window graphs generated after exposure and development of the grating samples. Since there are differing results for horizontally and vertically stacked gratings, different dose windows were generated for each case. In order to generate the graphs, the gratings were visually characterized using SEM images and the line doses corresponding to the lower and higher boundaries of the dose windows for quality patterns were determined by SEM inspection. Dose window graph illustrate the optimal dose regimes for which quality nanostructures can be fabricated at a given temperature and duration of development. In the Figures, the solid lower (blue and green) lines respectively show the minimum doses while the solid (red and purple) lines show the maximum doses at which good quality gratings can be obtained. Generally, if the dose window is wide, it means that the fabrication process has better

reproducibility and minor deviations from nominal process conditions would still result in successful structures. [32]

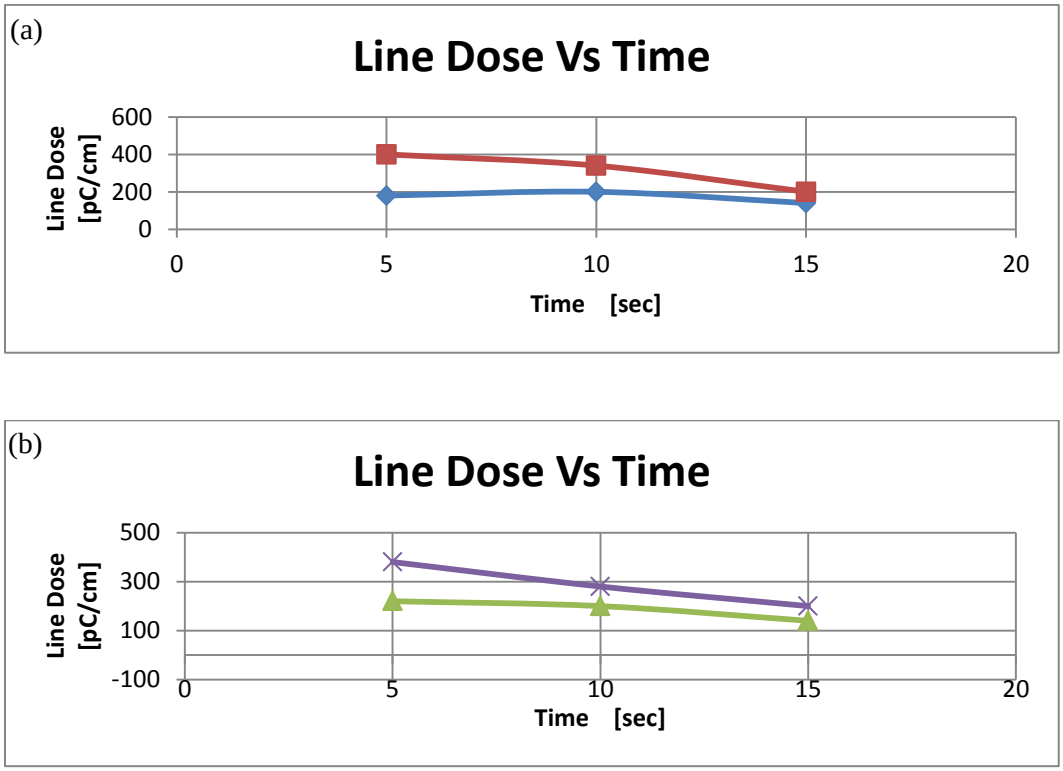

Figure 23: Example of dose window graphs for (a) 60 nm horizontally stacked gratings and (b) 60 nm vertically stacked gratings exposed with 1 keV energy and developed during 5 sec, 10 sec and 15 sec at -15 °C

4.3 **Sensitivity and Robustness**

I observed that both 1 keV and 2 keV exposures are limited in robustness.

Figure 24 compares the dose windows obtained for 1, 2, 3, 10 and 30 keV. The data used for 1 keV and 2 keV was obtained for 80 nm pitch gratings developed for 5 sec while 3, 10, and 30 keV data was taken from previous work [9] and obtained for 70 nm pitch gratings developed for 5 sec. By comparing the dose windows for the different energies, it can be observed that the dose window

increases with energy implying a more robust and reproducible process for fabrication. Hence, 10 keV EBL can be expected to be more reproducible than 1 keV EBL.

However, the resist is very sensitive due to more efficient energy deposition and relatively low doses were sufficient for exposure. From Figure 24, it can be seen that a line dose of 280 pC/cm - 400 pC/cm was required for exposure at 1 keV while a line dose of 450 pC/cm - 825 pC/cm was required for 2 keV for 80 nm pitch gratings and developed for 5 sec. At a higher energy of 10 keV, a much higher dose will be required comparing with data given in earlier work [9] where for 70 nm gratings at the same processing conditions, line doses of approximately 875 pC/cm - 2050 pC/cm was required for exposure. The lower dose resulted in very short exposure times, so the input pattern shown in Figure 16 (a) and ~7600 μm2 markers (not shown) could be exposed in 6 min 34 sec at 1 keV and 17 min 56 sec at 2 keV.

Figure 25 compares the average dose required for good exposure for 1, 2, 3, 10 and 30 keV. The data used for 1 keV and 2 keV was obtained for 80 nm pitch gratings developed for 5 sec (shown as squares) while 3, 10, and 30 keV (shown as dots) was again taken from previous work [9] and obtained for 70 nm pitch grating and development time of 5 sec. As in the case of Figure 24, the average exposure dose has a strong dependence on the exposure energy as shown by the linear behavior slope. One can conclude that, despite a loss in process robustness, ultra-low energy exposures present a strong advantage because of their high sensitivity.

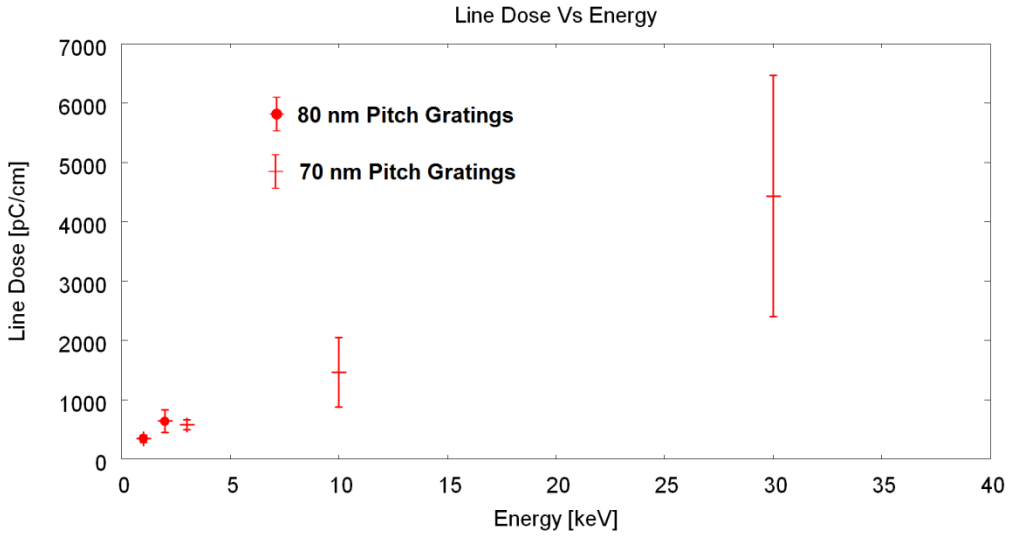

Figure 24: The applicable line dose windows as a function of exposure energy for 70 nm pitch gratings (3, 10, 30 keV) - shown as crosses - and 80 nm (1, 2 keV) gratings - shown as cross and spot. Samples were developed for 5 sec.

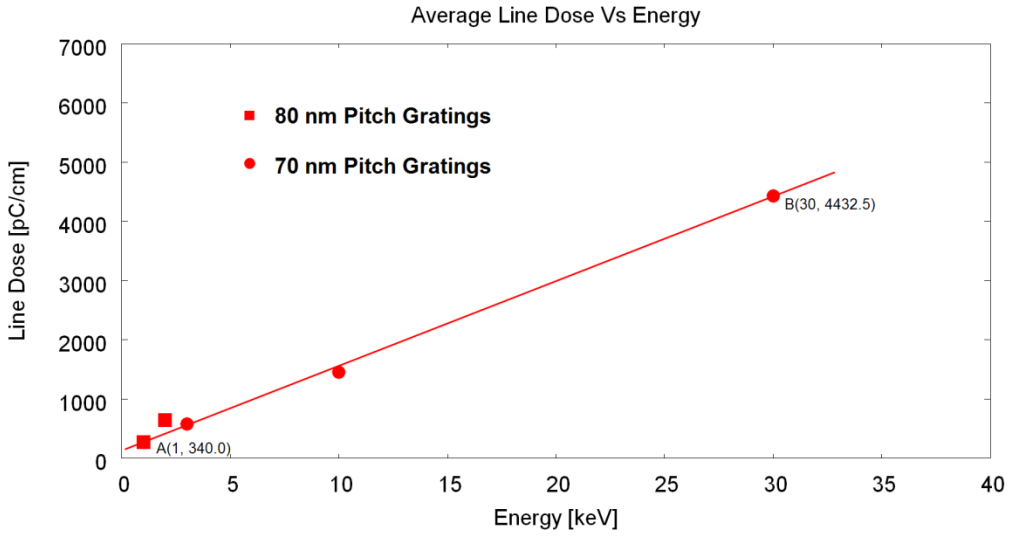

Figure 25: The applicable average line dose window as a function of exposure energy and a development time of 5 sec for 70 nm (3, 10, 30 keV) - shown as dots - and 80 nm (1, 2 keV) gratings - shown as squares. Samples were developed for 5 sec. The slope of the line of best fit is ≈ 141.12pC/cm•keV. The points were obtained using the plotting function of Gnuplot. [85]

4.4 **Comparative analysis of dose windows with ultra-low-voltage exposures**

In order to achieve a quantitative understanding of the relationship of the applicable dose window with the process conditions, dose window graphs have been generated for 1 keV and 2 keV EBL energies.

Dose test grating patterns as described in Sect. 3.3 and 4.2 were generated in the resist and evaluated using plan-view SEM micrographs to create dose window graphs. The regions of under exposure, good exposure and over exposure have been identified by visual inspection after which the line dose range corresponding to the start and the end of well-exposed gratings is plotted against the development time to generate the dose window graphs. For applications of ultra-low voltage exposures, the goal is to fabricate well-resolved, good quality structures; hence, a lot of the discussion revolves largely around these aspects.

4.4.1 **1 keV Experiments**

The experiments performed for 1 keV EBL are summarized in Table 2 and Table 3. Table 2 presents sets of experiments which were performed to fabricate nanostructures at 1 keV.

Table 2: Summary of Dose Windows obtained for 60 nm pitch gratings at 1 keV. Reported values are in pC/cm.

Development Time	**5 sec**		**10 sec**		**15 sec**		**20 sec**		
Orientation	Horizontal	Vertical	Horizonta	Vertical	Horizontal	Vertical	Horizontal	Vertical	Comments
Experiment 1	280-320	200-320	280-340	200-320	-	-	-	-	Basic, Step size = 10 nm
Experiment 2	240-360	240-360	200-320	200-240	160-360	200-320	120-160	-	Step size = 2 nm
Experiment 3	160-320	240-280	-	-	120-320	200-280	-	-	WF Size = 50 X 50 um

Table 3: Summary of Dose Windows obtained for 80 nm pitch gratings at 1 keV. Reported values are in pC/cm.

Development Time	5 sec		10 sec		15 sec		20 sec		
Orientation	Horizontal	Vertical	Horizonta	Vertical	Horizontal	Vertical	Horizontal	Vertical	Comments
Experiment 1	320-400	200-400	320-400	280-400	-	-	-	-	Basic, Step size = 10 nm
Experiment 2	280-400	280-400	120-160	120-200	160-400	200-360	120-160	120-360	Step size = 2 nm

The first experiment #1 was the initial experiment with the starting line dose of 80 pC/cm and resist thickness of 31 nm obtained by simulation using our EBL simulator as described in section 3.6. The basic experiment was the first experiment and it gave an idea of the working conditions of the Raith 150^{TWO} exposure system operating at 1 keV using a beam step size of 10 nm. The beam step size is the distance between adjacently located spots as the beam exposes each component of a fragmented pattern. So in writing a line, the system first fragments it into smaller spots, which are later exposed one spot at a time as determined by the beam step size. In order to write a very fine pattern, therefore, a smaller step between spots is required to make continuous well-defined patterns. The input patterns shown in Figure 16 (a) were written using the Raith 150^{TWO} EBL system but a smaller step size of 2 nm. Four sets of such patterns were exposed on a single silicon substrate, which was then cleaved and developed for 5 sec, 10 sec, 15 sec and 20 sec at -15 ºC. As shown in Table 2, there exists quite broad applicable dose windows to fabricate 60 nm pitch gratings at 1 keV exposure under different sets of processing conditions. Experiment #2 produced a larger and more robust dose window than experiment #1 by changing the step size from 10 nm to 2 nm. This leads to improved exposure as a finer pattern is written due to the smaller step size. In experiment #3, the write field was reduced from

100 × 100 µm to 50 × 50 µm and the effect of this is described in section 4.6. It can be seen that, for 60 nm pitch gratings, there is a wide range of doses for fabricating gratings at 1 keV.

Table 3 shows the results obtained for 80 nm pitch gratings fabricated at 1 keV and developed for various durations. Like previously shown, there also exists a significant dose window for fabricating 80 nm pitch structures under different conditions.

Figure 26 shows high resolution SEM micrographs of developed grating structures. These micrographs are representative of quality patterns in 31 nm PMMA fabricated using 1 keV EBL and developed at -15 ºC. Figure 26 (a) shows 60 nm pitch horizontally stacked gratings fabricated on 31 nm thick PMMA layer using a line dose of 160 pC/cm and developed for 15 sec and Figure 26 (b) shows 60 nm pitch vertically stacked gratings fabricated on 31 nm of PMMA using a line dose of 320 pC/cm and developed for 5 sec. Figure 26 (c) shows 80 nm pitch horizontally stacked gratings fabricated on 31 nm PMMA thick layer using a line dose of 240 pC/cm and developed for 15 sec, Figure 26 (d) shows 80 nm pitch vertically stacked gratings fabricated using a line dose of 320 pC/cm and developed at -15 ºC. The grating morphologies for the well-exposed gratings shown in Figure 26 exhibit a clear line-spacing-line structure that is well defined and have a high contrast.

Figure 27 shows the graphical plot of the applicable dose window as a function of the development time at cold temperatures of -15 °C. It can be seen from this

figure that longer development time decreases the window for which quality gratings could be fabricated. Thus, at 5 sec, there is an adequate window which reduces to the point by 20 sec development time, no gratings structures could be fabricated. Also, by examining Table 2 and Table 3, it can be seen that the applicable dose exposures windows for horizontally stacked and vertically stacked features are somewhat different.

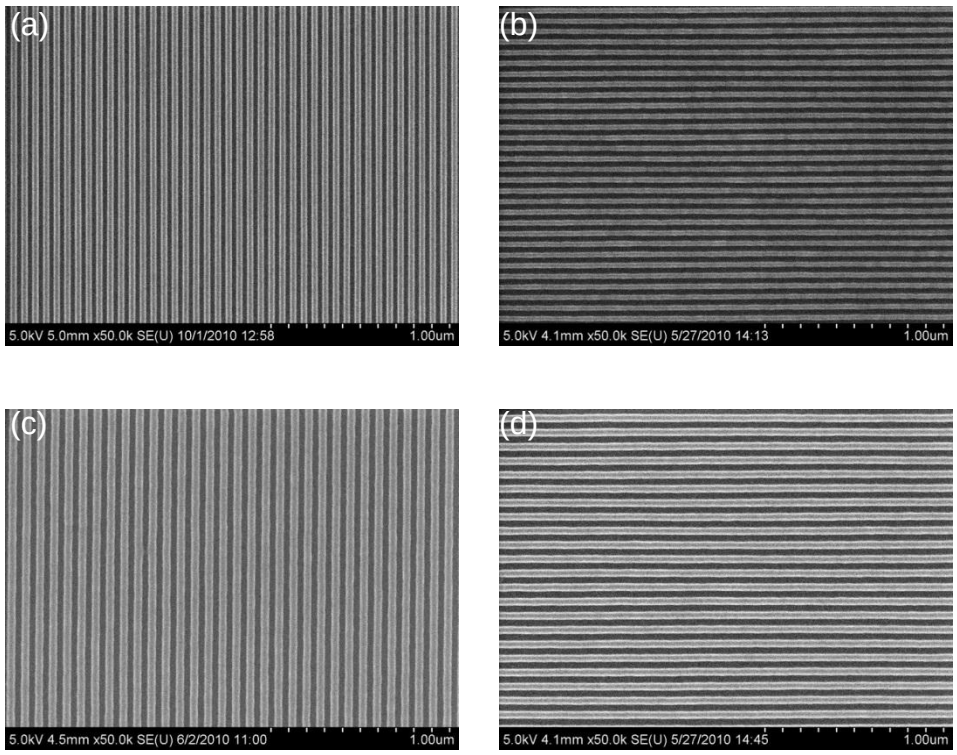

Figure 26: Examples of high resolution nanostructures fabricated at 1 keV (a) 60 nm horizontally stacked and (b) vertically stacked gratings; (c) 80 nm horizontally stacked and (d) vertically stacked gratings.

The differences in exposure dose window for horizontally stacked and vertically stacked gratings is possibly due to beam instability issues at low energies resulting in different levels of exposure of gratings of identical geometry but

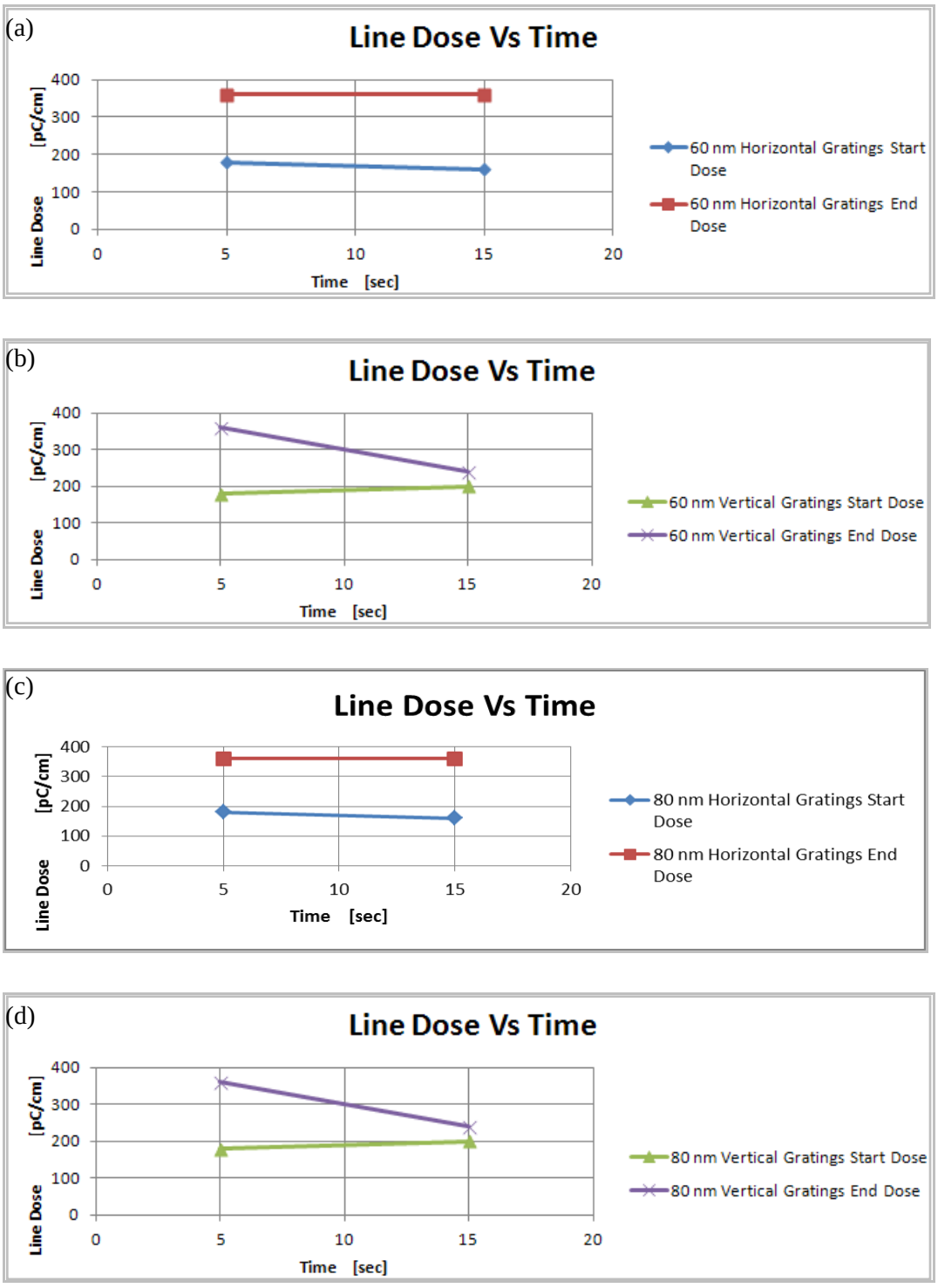

Figure 27: Example of dose window graphs for 60 nm (a) horizontally stacked and (b) vertically stacked gratings; and 80 nm (c) horizontally stacked and (d) vertically stacked gratings fabricated with 1 keV exposures of 31 nm thick PMMA layers, and developed at -15 ºC during various times.

different orientations. This is further discussed in section 4.6. This may suggest that features in either direction received a slightly different dose, which might be because of beam instability issues in the patterning tool at ultra-low voltages. It can be seen that the dose window for vertically stacked features is slightly larger than the dose window for horizontally stacked features.

An important conclusion is that although ultra low voltage lithography is more challenging than higher voltages, [9, 30] the result show that there exist reasonably broad process windows which allow for fabrication of good quality structures.

4.4.2 **2 keV Experiments**

The experiments performed for 2 keV exposures at 60 nm and 80 nm are summarized in Table 4 and Table 5 respectively. The input pattern shown in Figure 16 (b) was written using the Raith 150^{TWO} EBL system. The beam step size used was 2 nm as discussed earlier in section 4.3.1 and the samples were developed for 5 sec and 15 sec. Based on EBL simulator results using PMMA thickness of 37 nm, a starting line dose of 300 pC/cm was used. These tables show two sets of data under nominally the same conditions to check the repeatability of the process. As can be observed, the applicable doses for fabricating gratings were generally similar with some minor variations as a larger dose window was observed at the second run of the experiment. This variation is possibly due to beam stability issues causing slight differences in exposure during the first and second run of the experiment. As shown in Table 4 and Table 5, nanostructures can be fabricated in a wide dose window at 2 keV.

Table 4: Summary of Dose Windows obtained for 60 nm pitch gratings at 2 keV. Reported values are in pC/cm.

Experiment #	5 sec		15 sec		
	Horizontal	Vertical	Horizonta	Vertical	Comments
1	300-450	300-450	300-410	300-410	Basic
2	450-525	450-525	375-390	300-400	Repeated

Table 5: Summary of Dose Windows obtained for 80 nm pitch gratings at 2 keV. Reported values are in pC/cm.

Experiment #	5 sec		15 sec		
	Horizontal	Vertical	Horizonta	Vertical	Comments
1	450-825	450-825	300-750	450-710	Basic
2	450-825	450-900	300-675	450-675	Repeated

Figure 28 shows high resolution SEM micrographs of 60 nm horizontally stacked, 60 nm vertically stacked, 80 nm horizontally stacked and 80 nm vertically stacked gratings respectively. These micrographs are representative of quality patterns fabricated using 2 keV exposures. Figure 28 (a) shows 60 nm pitch horizontally stacked gratings fabricated on 37 nm of PMMA using a line dose of 300 pC/cm and developed for 5 sec -15 ºC, Figure 28 (b) shows 60 nm pitch vertically stacked gratings fabricated in 37 nm thick layer of PMMA using a line dose of 300 pC/cm and developed for 5 sec at -15 ºC, Figure 28 (c) shows 80 nm pitch horizontally stacked gratings fabricated in 37 nm thick layer of PMMA using a line dose of 600 pC/cm and developed for 5 sec at -15 ºC, and Figure 28 (d) shows 80 nm pitch vertically stacked gratings fabricated in 37 nm thick layer of PMMA using a line dose of 450 pC/cm and developed for 5 sec at -15 ºC. The grating morphologies for the well-exposed gratings at 2 keV shown in Figure 28 (a-d) exhibit periodic structure that is well defined and have a high contrast.

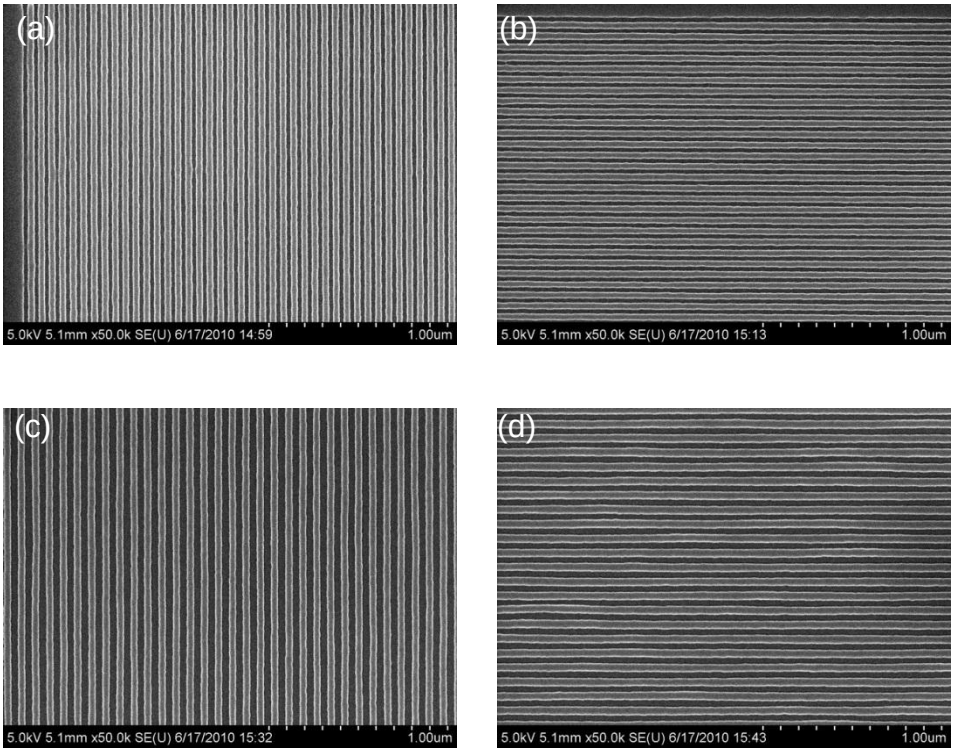

Figure 28: Examples of high resolution nanostructures fabricated at 2 keV exposure 60 nm (a) horizontally stacked gratings and (b) vertically stacked gratings, 80 nm (c) horizontally stacked and (d) vertically stacked gratings. The initial PMMA layer was 43 nm and developed at -15 ºC

Figure 29 (a-d) shows the graphical plot of the applicable dose window for selected development times at cold temperatures of -15 °C. The same conventions as used for the graphs in the previous sub-section were adopted: the solid lines (with diamond and triangle connectors) show the minimum dose while the solid lines (with square and x connectors) show the maximum doses required to obtain good quality gratings. This is the region bounded by the lines denoted "Start Dose" and "End Dose". Exposures below the minimum dose resulted in under exposed features while those above the maximum dose applicable produced over exposed features.

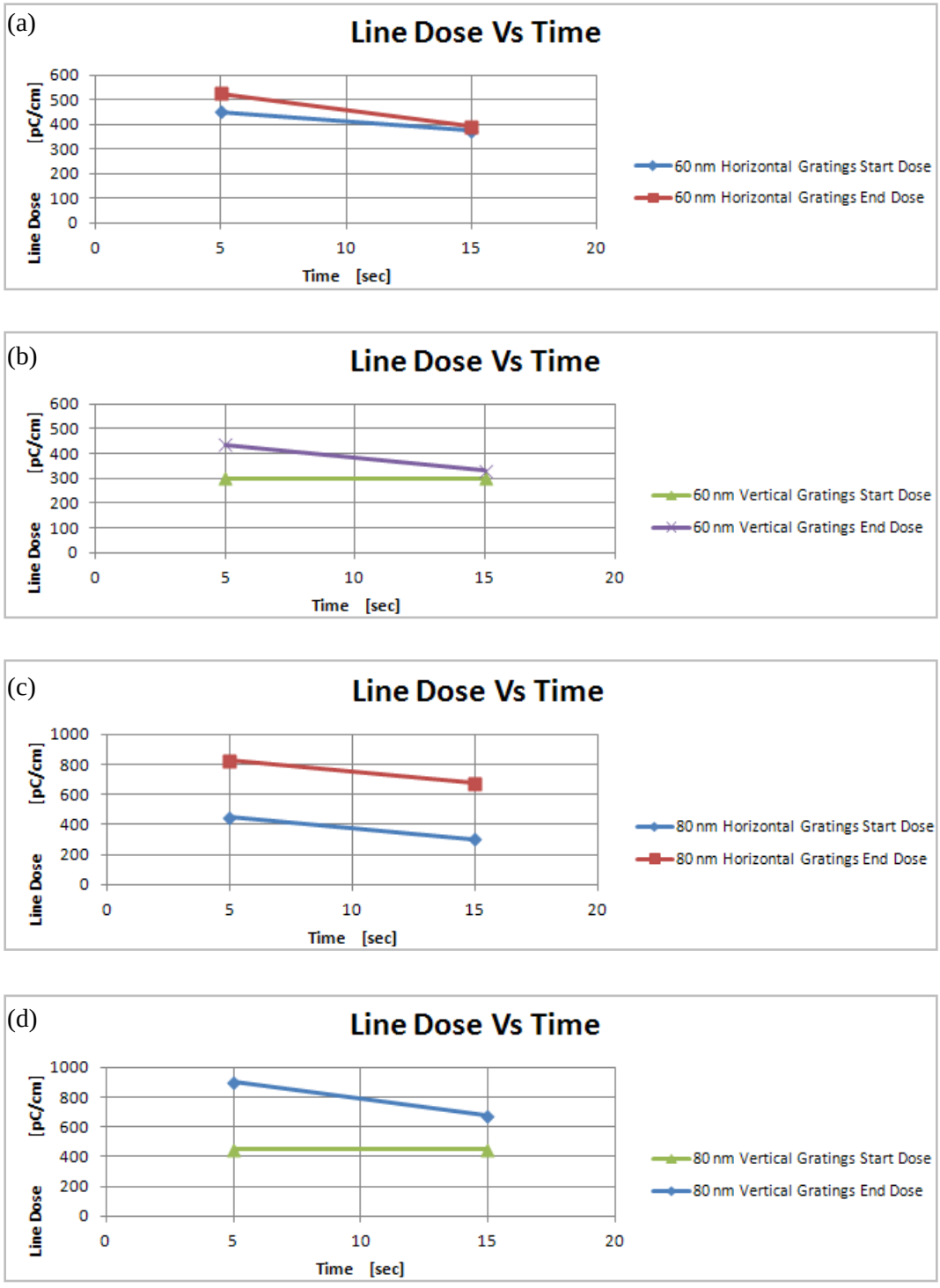

Figure 29: Example of dose window graphs for 60 nm (a) horizontally stacked and (b) vertically stacked gratings, 80 nm (c) horizontally stacked and (d) vertically stacked gratings fabricated with 2 keV exposures of 37 nm thick PMMA layers, and developed at -15 ºC during 5 sec and 15 sec.

It can be seen that the trend shown by the graphs in Figure 29 (a-d) agree with that obtained for 1 keV EBL and shown in Figure 29 (a-d). In particular, longer development time narrows the dose window for which quality gratings could be fabricated. Also, from Figure 29 and data presented in Table 4 and Table 5, it is evident that the applicable dose windows for horizontally stacked and vertically stacked features are different as in the case of 1 keV exposures. However, this difference is somewhat less pronounced as shown in Table 3 for 80 nm pitch gratings. Further discussion of this is given in section 4.3.3. Overall, the results indicate that there is a broader process window, which allows for fabrication of good quality structures at 2 keV exposures.

4.5 **Metrology of fabricated nanostructures**

Representative nanostructures fabricated at 1 keV and 2 keV exposures and shown in Figure 30 were characterized by size measurements using the metrology capability of the Quartz PCI software in which several lines were measured and the mean line width and standard deviations were calculated. For 60 nm pitch gratings fabricated at 1 keV, the mean line width was 27.2 ± 2.9 nm for horizontally stacked gratings while the minimum line width for vertically stacked gratings was 28.3 ± 2.2 nm. For 80 nm pitch gratings fabricated at 1 keV, the mean line width for horizontally stacked gratings was 33.1 ± 1.7 nm while for vertically stacked gratings, it was 34.1± 2.3 nm. For 60 nm pitch gratings fabricated at 2 keV, the mean line width was 21.0 ± 3.3 nm for horizontally stacked gratings while the minimum line width for vertically stacked gratings was 22.6 ± 1.6 nm. For 80 nm pitch gratings fabricated at 2 keV, the mean line width

for horizontally stacked gratings was 35.7 ± 2.2 nm while for vertically stacked gratings, it was 33.4 ± 3.9 nm.

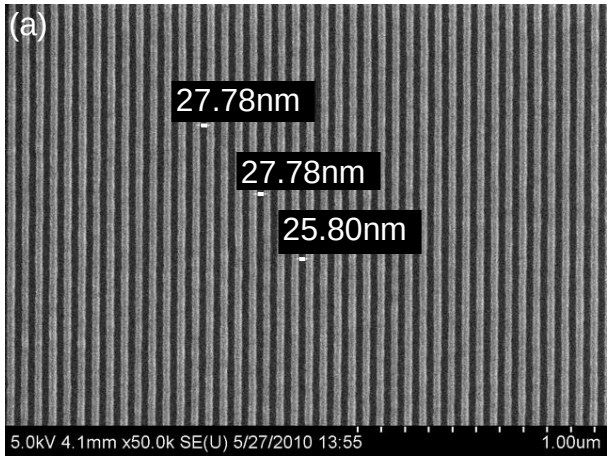

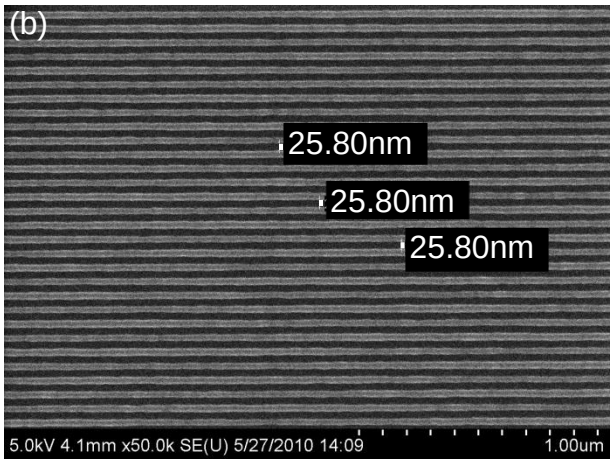

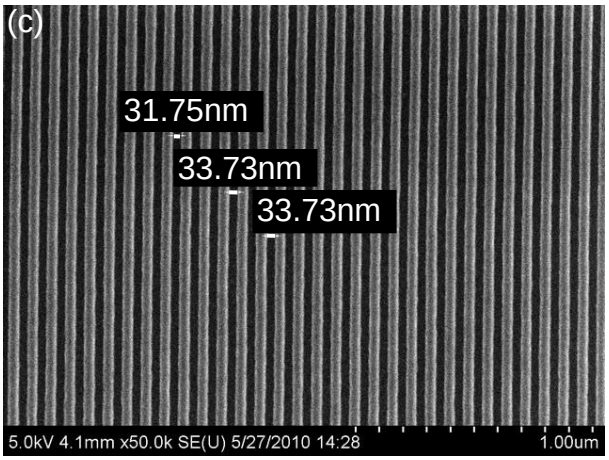

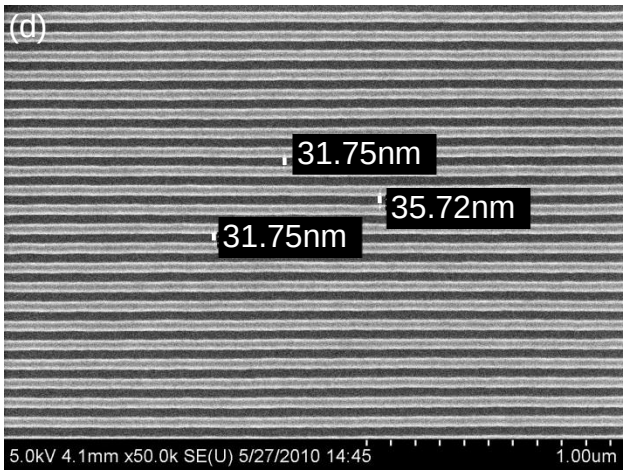
(d)
31.75nm
35.72nm
31.75nm
5.0kV 4.1mm x50.0k SE(U) 5/27/2010 14:45
1.00um

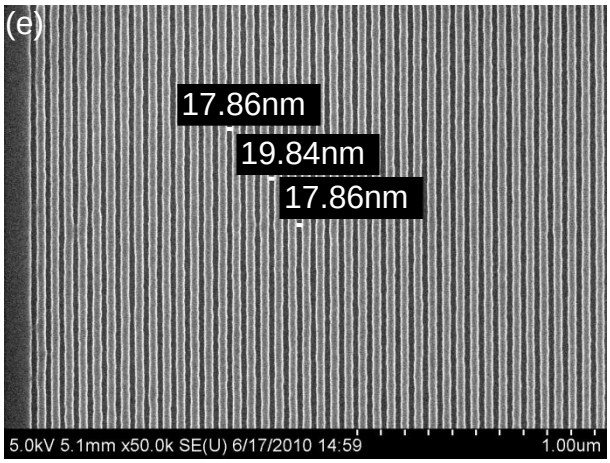
(e)
17.86nm
19.84nm
17.86nm
5.0kV 5.1mm x50.0k SE(U) 6/17/2010 14:59
1.00um

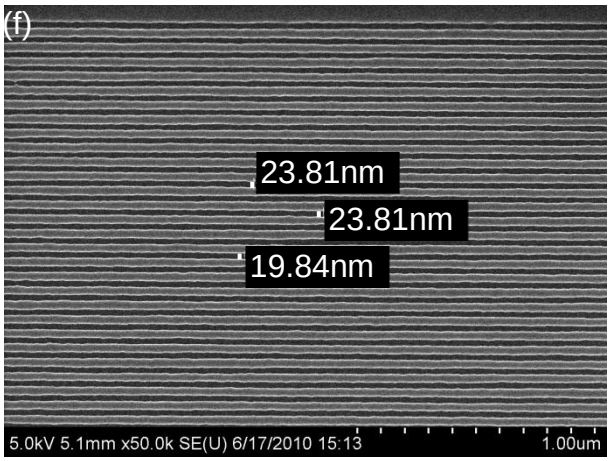
(f)
23.81nm
23.81nm
19.84nm
5.0kV 5.1mm x50.0k SE(U) 6/17/2010 15:13
1.00um

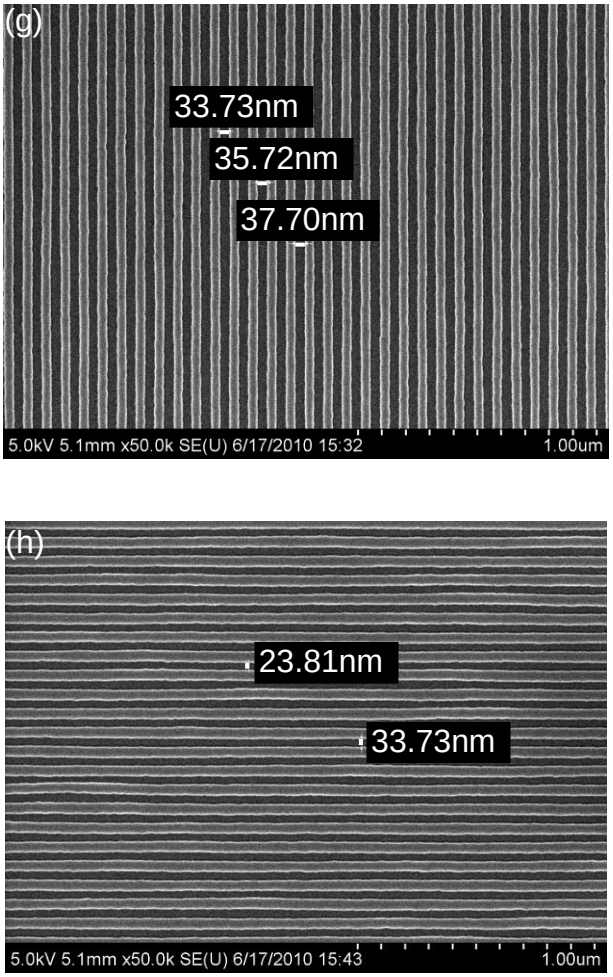

Figure 30 (a-h): Example of measured line widths (a) 60 nm horizontally stacked gratings fabricated at 1 keV on 31 nm of PMMA resist (b) 60 nm vertically stacked gratings fabricated at 1 keV on 31 nm of PMMA resist (c) 80 nm horizontally stacked gratings fabricated at 1 keV on 31 nm of PMMA resist (d) 80 nm vertically stacked gratings fabricated at 1 keV (e) 60 nm horizontally stacked gratings fabricated at 2 keV on 37 nm of PMMA resist (f) 60 nm vertically stacked gratings fabricated at 2 keV on 37 nm of PMMA resist (g) 80 nm horizontally stacked gratings fabricated at 2 keV on 37 nm of PMMA resist (h) 80 nm vertically stacked gratings fabricated at 2 keV on 37 nm of PMMA resist.

4.6 **Beam Stability Challenge**

During the initial experiment (basic), the results indicated a certain non-uniformity of exposure between horizontally stacked and vertically stacked gratings as well as gratings with the same orientation but written at different locations within the write field. Generally, vertically stacked features were better exposed than horizontally stacked ones suggesting that they might have received a higher electron dose. To resolve or minimize these effects, the beam step size was changed from the default 10 nm to 2 nm. This somewhat reduced the effect at 1 keV but did not eliminate it entirely.

In order to observe if this issue also occurred at other voltages, the pattern shown in Figure 16 (a) was exposed at 10 keV and also at 2 keV and developed and processed under similar conditions as 1 keV samples. It was observed that the effect was virtually absent at 10 keV but quite evident at 2 keV. In addition to the change in beam step size from 10 nm to 2 nm, the write field size was also reduced from 100 µm × 100 µm to 50 µm × 50 µm and the pattern was written as close to the center of the write field as possible. The intention of this was to reduce the beam deflection to smaller angles within the write field. This change improved results at 1 keV, and 60 nm pitch gratings developed for 15 sec were more uniform and better resolved. This can be seen in Figure 31(a) which shows unresolved features while Figure 31(b) shows the same gratings but with a reduced write field size of 50 µm x 50 µm showing well resolved gratings. However, features located away from the center of the write field still were of lower quality compared to those written closer to the center of the write field.

This can be seen in Figure 32 where features away from the center of write field are somewhat over-exposed while the exactly same features with the same processing conditions but closer to the center of the write field are more uniformly exposed. Figure 32 (g) shows the position of each exposure relative to the write field. Figure 32 (a) and (f), corresponding to locations 1 and 6 are farther from the center of the write field and are over-exposed as the formation of negative tone PMMA and density multiplication are observed. Figure 32 (c) and (d) are most uniformly exposed while Figure 32 (b) and (e) are slightly more exposed.

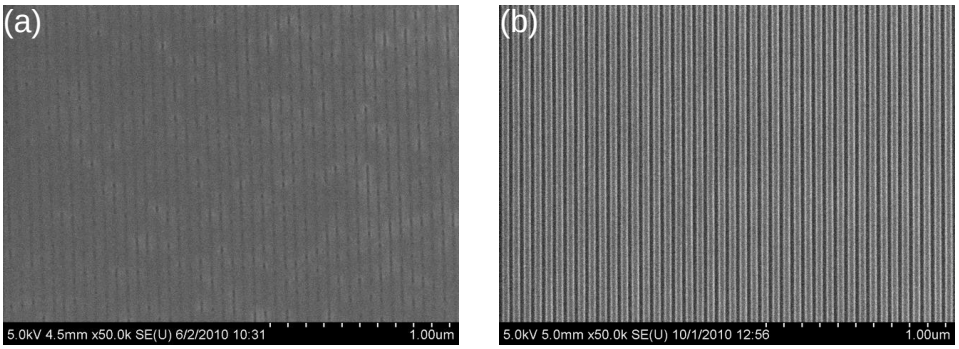

Figure 31: Example of high resolution nanostructures fabricated at 2 keV exposure - (a) 60 nm horizontally stacked gratings (b) 60 nm vertical vertically stacked gratings

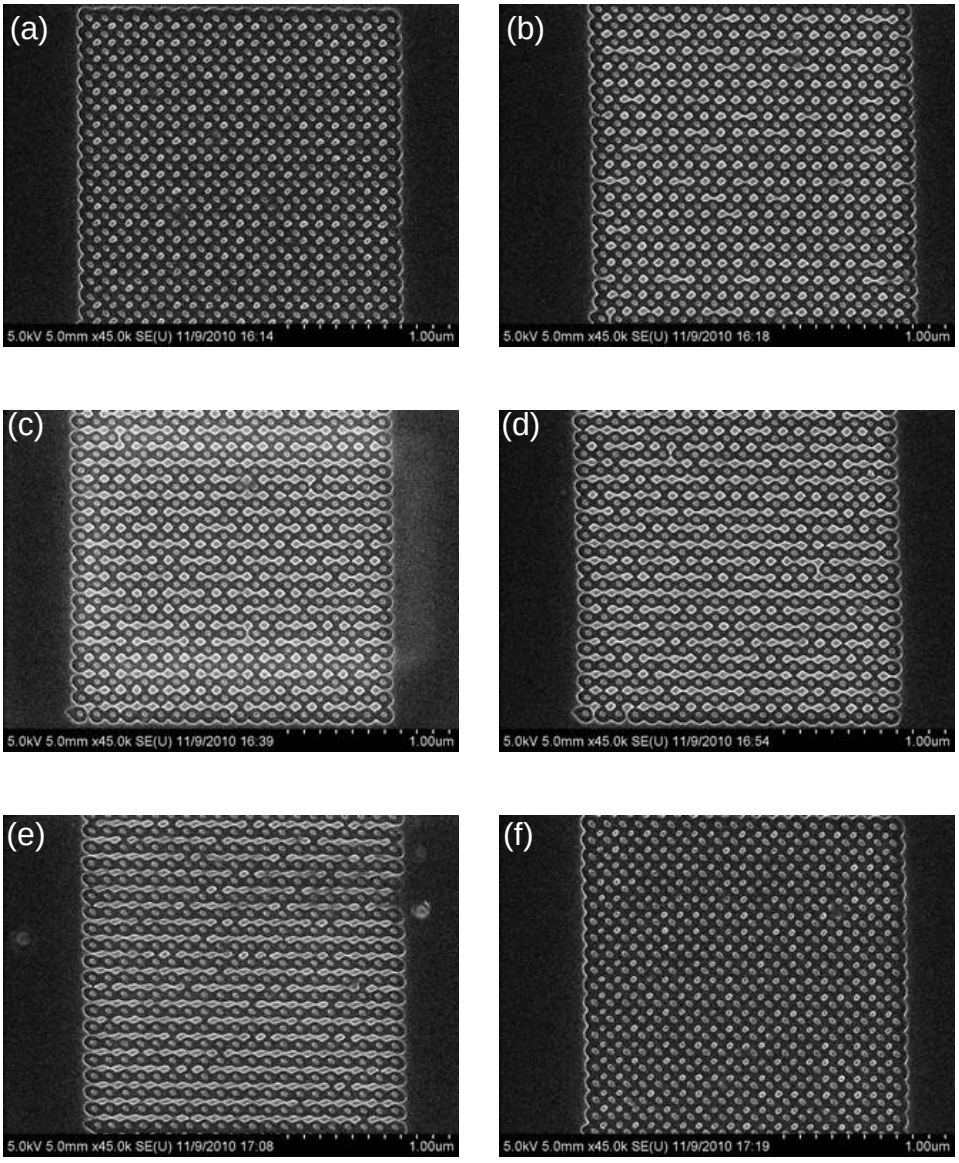

Figure 32: Non-uniformity of exposure depending on location relative to the center of the write field. Arrays of dots labeled (a-f) span the diagonal from the bottom right to top left .

5 Density Multiplication of Nanostructures[2]

5.1 Introduction

Double patterning is an example of density multiplication whereby the number of patterned structures is a multiple of that which could be achieved by any one nominal exposure. The processes that have been used to achieve such double patterning include the dual line approach or dual trench approach in which a single design is split into two separate designs and the pattern is transferred into the underlying layer after lithography-etch-lithography-etch processes. [86, 87] Other approaches which are also based primarily on conventional lithography are self-aligned spacer, [87, 88, 89] dual-tone resist [90], dual-tone development [87, 91, 92] and litho-process-litho-etch. [87] These methods are top-down processing techniques. Another approach that has been used to achieve density multiplication is the bottom-up approach of self-assembly when a pattern generated by electron beam lithography (EBL) is converted into a denser structure by directed assembly of block co-polymers. [20, 15, 7, 8]

The different approaches to achieve pattern density multiplication [86, 20, 15] require the described multiple lithographic or processing steps such as block co-polymer assembly. However, density multiplication of nanoscale patterns can be achieved in a more straightforward way that does not involve directed assembly of block co-polymers or multiple lithographic or post processing steps. In this approach, a carefully optimized, single EBL process was employed to fabricate denser

[2] *A version of this chapter has been published. J. Vac. Sci. Technol. B 29, 06F312 (2011); doi:10.1116/1.3657512.*

features than in the original patterns comprising arrays of dots and single pixel lines.

For positive-tone resists such as polymethylmethacrylate (PMMA), the electron bombardment causes scission of molecular bonds of the polymer. After exposure the polymer chains are broken into more soluble fragments of reduced molecular weights. During development, the exposed areas readily dissolve in a solvent (developer). Most applications employ PMMA responding as a positive-tone resist.[21, 22, 32, 30, 11, 33] However, if PMMA is exposed at a dose several times higher than that required for the positive-tone response, polymer cross-linking starts to occur.[34, 36, 37, 38, 39, 35]After the development stage, patterns of overexposed cross-linked PMMA would remain, thus behaving as a negative-tone resist. The detailed molecular mechanism behind the negative-tone response of PMMA is a theme of ongoing discussions. In a number of works, the high dose electron beam irradiation of PMMA has been proposed to result in a carbonization process [34, 36, 37, 38, 39, 35] rather than a cross-linking of the PMMA fragments. However, there is no doubt that in appropriate exposure regimes, PMMA can behave as both a positive-tone and a negative-tone resist. In the light of the allusions made in, [22, 93, 94] it is quite natural to assume that it may be possible to fabricate both negative-tone and positive-tone patterns in PMMA in a single exposure and development process step. This capacity of PMMA is exploited in the present work.

Figure 33 illustrates density multiplication using an initial pattern composed of an array of dots and lines in Figure 33 (a) to be generated in a resist. After density

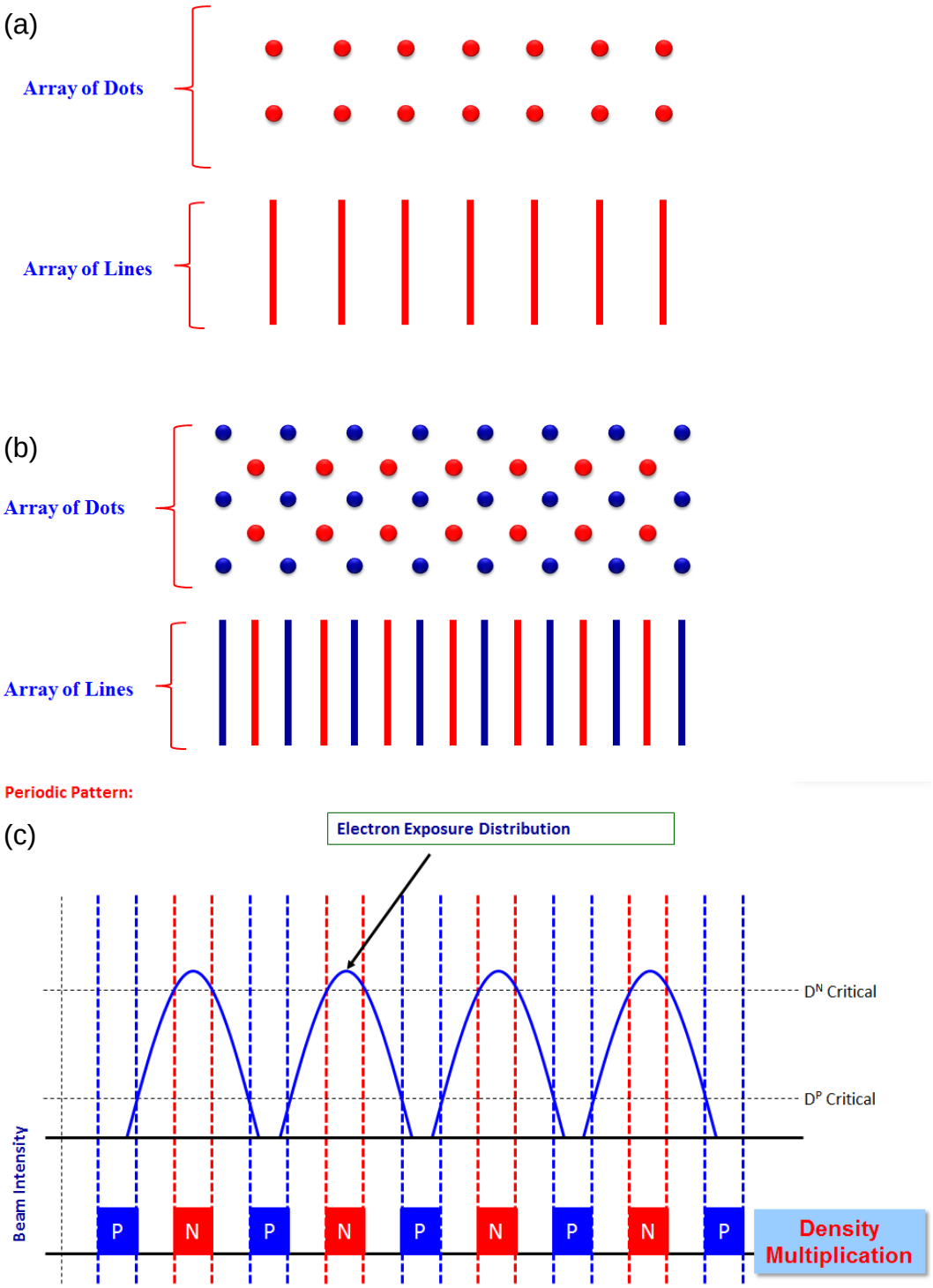

Figure 33: Density Multiplication (a) Initial Pattern (b) Multiplied pattern (c) Graphical description of how density multiplication works

multiplication, a denser pattern with approximately double the number of features is generated on the final pattern as shown in Figure 33 (b). Figure 33 (c) describes the process of density multiplication for a periodic pattern. A periodic pattern is that with structures of similar geometry equi-spaced at defined intervals. In the centers of the beam spots at a sufficient intensity that is required for cross-linking of PMMA (D^N Critical), negative-tone response of PMMA occurs while at the periphery of successive beam spots, PMMA responds as a positive-tone resist (D^P Critical). This results in an array of structures of both positive-tone and negative-tone PMMA.

A challenge of the usage of PMMA as a negative tone EBL resist is that relatively high exposure doses are required. We believe that this disadvantage could be offset by decreasing the voltage of exposure, since this results in an increase of the sensitivity. [30] The usage of low voltage exposures, however, requires compatible development conditions in order to achieve a robust pattern fabrication at deep nanoscale. It has been demonstrated previously [32, 30] that the resolution of low-voltage EBL processing of PMMA can be improved if the development temperature is decreased. However, no attempt to combine these optimized processes with the usage of PMMA as both positive-tone and negative-tone resist has been reported to date.

In this work, we report the fabrication of structures at the deep nanoscale employing an ultra-low voltage of 1 keV combined with cold development, and report the resulting nanostructures composed of dots and lines. We have successfully achieved a density doubling in dot pattern arrays with an initial pitch

of 80 nm as well as in a grating pattern initially with a 100 nm pitch with a single exposure and development EBL process step. The resulting structures have a pitch half as large as that nominally written. Furthermore, we have explored the possibility to apply this density multiplication approach to fabricate more complex patterns than arrays of dots and lines.

5.2 **Experiment**

Silicon wafers (100) were diced to 1.5 cm × 1.5 cm size and cleaned in Piranha (75% sulphuric acid and 25% hydrogen peroxide) for 15 minutes to remove organic residues. The wafers were rinsed in the dump rinser in a 5-cycle rinse process. Then, the wafers were blown dry and pre-baked at ~175°C for 5 minutes on a hot plate to drive-off residual water molecules and dry the samples. Next, the wafers were spin-coated with 950K PMMA using a Headway Spinner to form films of 30 – 43 nm thickness on the silicon wafers and soft-baked on a hot plate at ~175°C for 5 minutes after which they were allowed to stand for several minutes to cool down. The thicknesses of the resist coating were measured using the VASE Ellipsometer or Filmetrics Resist and Dielectric Thickness Mapping System.

The next step was to make electron beam exposure using a Raith 150^{TWO} instrument using writing patterns created with the Raith 150 GDS II software. Several patterns that were exposed in this work are shown in Figure 17(a – c, e). Ultra-low energy exposure of 1 keV was employed in order to reach higher process sensitivity.

In order to determine the optimal point and line exposure doses required to achieve the density multiplication, special dose tests were performed. Figure 17 (a) illustrates one of array designs composed of 50 × 50 dots. For this design,80 nm and 100 nm inter-dot spacing were employed. Multiple arrays of the 50 × 50 dot patterns were written on a single wafer with assigned exposure doses varying from 1.25 - 13.75 fC/dot for 80 nm dots and 3.33 - 36.63 fC/dot for 100 nm pitch dots. In the case of gratings shown in Figure 17 (b), the dose test comprised an array of 10 μm long lines spaced by 100 nm, with the line dose increasing from 1000 pC/cm to 5000 pC/cm. The dose increment between two neighboring lines was 0.2% in order to generate locally constant dose conditions. Figure 17 (d) and Figure 17 (e) show 100 nm pitch lines in a cross configuration and T-junction arrangement. For these designs, 5 copies of each were written and assigned doses varying from 1600 pC/cm to 2200 pC/cm.

After exposure, the wafers were developed in an methyl isobutyl ketone: isopropyl alcohol (MIBK:IPA) 1:3 mixture for 5 sec, 10 sec and 15 sec. Following the approach reported earlier, [32, 30] the development temperature was maintained at the level of -15 °C or -20 °C using a cold plate (Stir Kool SK-12D, Ladd Research). After development, the samples were rinsed in IPA, acting as a stopper, for 10 sec or 20 sec at the same temperature in order to compare the morphologies of the developed nanostructures. An approximately 5 nm thick layer of Cr was deposited on the developed samples as an anti-charging layer using a Gatan Sputtering System before surface imaging in a Hitachi S-4800 Field Emission scanning electron microscope (SEM). Then, the morphologies were

observed using SEM, and the results from the different development conditions were compared to determine the optimal dose, development time and temperature. These parameters were finally used to fabricate structures to achieve the density multiplication.

5.3 **Modeling**

In order to better understand the underlying mechanism, we have conducted detailed modeling of exposure in PMMA employing our EBL simulation tool reported recently. [12] In brief, in our model travel of primary, secondary, and backscattered electrons in PMMA is described by kinetic transport theory, [12, 13] which is numerically highly robust. In addition, to account for elastic scattering of primary electrons, the model also employs improved cross-sections for inelastic collisions, [13] which were validated against dielectric-response modeling. [13, 93] To account for scissions of bonds in PMMA by inelastic collisions, we compute the probability of dissociation of the main-chain C−C bonds accounting for molecular properties of PMMA's monomers such as the number of valence electrons and bond dissociation energies. This approach produces the yield of bond scission in PMMA directly without mapping the distributions of deposited energy, which avoids the well-known uncertainties related to the conversion of average deposited energy into a chemical response of the resist. More details about the model are given elsewhere. [13, 93] The simulator provides three-dimensional (3D) distributions, with a 1 nm resolution, for the yields of scission of the main chain in PMMA per monomer, for a given thickness of PMMA, substrate material, and exposure conditions. Previously, this simulation tool has been proven to predict

reasonably the response of PMMA in the positive-tone regime. [93, 94] Presently, the simulator does not yet include a complete modeling of the cross-linking of PMMA when it responds as a negative-tone resist; however, it is possible to compute the spatial distribution of the yield of scission for the exposure patterns of interest, and analyze the nominal yields of scission that correspond to the conditions where cross-linking is observed.

As an example, Figure 34 (a,b) show the cross-sections of a 3D distribution of the yield of scissions per monomer for a periodic array of single-pixel dots with a 100 nm pitch in a 30 nm thick layer of PMMA, simulated using 1 keV exposure with a dose of 30 fC/dot. For visualization purposes, the distributions in Figure 34 have been normalized so that white color corresponds to the highest yield of scission encountered in the image. In the following discussion, however, we report and analyze the actual yields of scission that are produced in periodic dot and gratings patterns at conditions that are similar to those used in experiments.

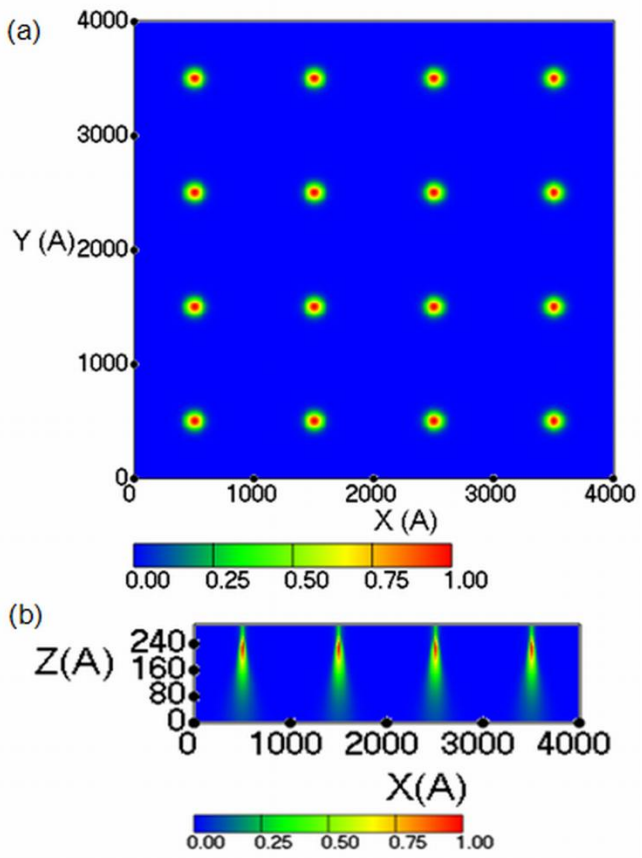

Figure 34: Two dimensional cross-sections of the predicted 3D distributions of the yield of main chain scissions per monomer in PMMA in a periodic array of single pixel dots employing 1 keV exposure of a 30 nm thick layer of PMMA on a Si substrate with a point dose of ~ 33.3 fC/dot; (a) the lateral X-Y distribution of the yield of scissions per monomer at the bottom of the resist layer; (b) a distribution of the yield of scission in the X-Z plane. The plots illustrate relative (normalized) distributions of the scission yield. In the legend, 1.00 corresponds to the maximum scission yield in the image. The dimensions are in angstroms.

5.4 **Results: Density Multiplication of Nanostructures**

In this section, selected experimental results of density multiplication and comparison with modeling of exposure for similar conditions are discussed.

The optimal dose window for exposing PMMA using 1 keV electrons and cold development was carefully determined using an array of dots and single pixel lines with dose variation. Next, the input patterns using were generated on the resist using the appropriate dose and cold development temperatures of -15 ºC or -20 ºC to fabricate denser features than in the original pattern.

Density doubling in dot pattern arrays with an initial pitch of 80 nm as well as in a grating pattern initially with a 100 nm pitch with a single exposure and development EBL process step was achieved in my work. The resulting structures have a pitch half as large as that nominally written. Furthermore, the possibility to apply this density multiplication approach to fabricate more complex patterns than arrays of dots and lines was explored.

The micrographs in Figure 35 show the evolution of fabricated nanostructures in PMMA when the exposure dose is increased from 3.33 fC/dot to 36.63 fC/dot. When PMMA responds as a positive-tone resist, polymer is removed from exposed locations, which results in the formation of holes at these locations. However, at a dose of approximately 10 fC/dot, round nano-sized dots of negative tone PMMA are formed in the center of the holes as shown in Figure30(a). At this point dose, some cross-linking of PMMA fragments around the center of the electron beam occurs while in the periphery of the beam spot, where the local intensity of exposure is reduced, PMMA still responds as a positive-tone resist. When the dose increases to 20 fC/dot (Figure 35 (b)), the dots of PMMA in the center increase in size due to stronger cross-linking and possibly carbonization of PMMA, while more of the resist in the periphery exposed by scattered electrons is

removed during development. Figure 35 (b-d) show how the nanostructures evolve when the dose increases.

Figure 35 shows representative SEM micrographs of an initially 100 nm × 100 nm pitch array of single pixel dots exposed with 1 keV electrons in a 30 nm thick PMMA layer on a Si substrate, employing the doses of 9.99 fC/dot, 20 fC/dot, 33 fC/dot, and 37 fC/dot; and developed at a temperature of –15 ºC for 5sec. At a point dose of approximately 33 fC/dot, a balance of positive and negative tone responses of PMMA produces an almost perfect array of dots of PMMA both in exposed and unexposed spots all across the resist layer. As a result, the areal density of the dots is doubled in comparison to the initial exposure pattern, as shown in Figure 35 (c). In Figure 35 (d), it can be seen that increasing the exposure dose further increases the size of the dots resulting from negative-tone response of PMMA, whereas the dots of the partially exposed undeveloped PMMA decrease in size.

Furthermore, Figure 35 (d) demonstrates that a control over the feature sizes can be achieved by varying the exposure dose as required. The capability of PMMA to respond in this interesting way is in part due to the broadening of the electron beam as illustrated by Figure 35 (b), which demonstrates that the exposure is stronger at the center of the beam and tapers out as the distance from the center increases. At some points, the intensity is above the threshold for negative tone behavior and at other locations it is below the threshold for positive tone behavior, allowing two different regions of polymer to exist after development.

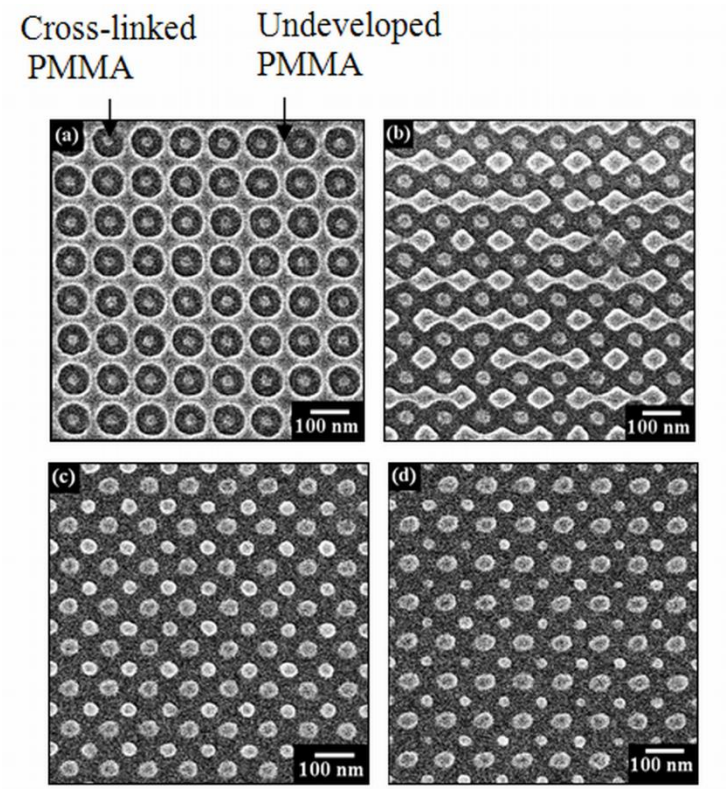

Figure 35: SEM images of an initially 100 nm×100 nm pitch array of single pixel dots exposed with 1 keV electrons in a 30 nm thick PMMA layer on a Si substrate, and developed at –15 °C for 5 sec. The panels correspond to point doses of (a) 9.99 fC/dot, (b) 19.98 fC/dot, (c) 33.30 fC/dot, and (d) 36.63 fC/dot. Panels (a) and (b) show both regions where PMMA is cross-linked, responding as a negative-tone resist, and regions of undeveloped PMMA. Panels (c) and (d) illustrate the density multiplication with a capacity of control over the features size by dose variation.

In addition to the dot arrays with initial pitch of 100 nm, we also obtained density multiplication of an initially 80 nm pitch dot array. Figure 36 (a) shows a high magnification plan view SEM micrograph of PMMA dots with density multiplication, fabricated using an initially 80 nm pitch array of exposure spots in a 43 nm thick PMMA layer on Si substrate. In this example, 1 keV exposure was employed with the dose of 12.5 fC/dot, and developed in an MIBK:IPA 1:3

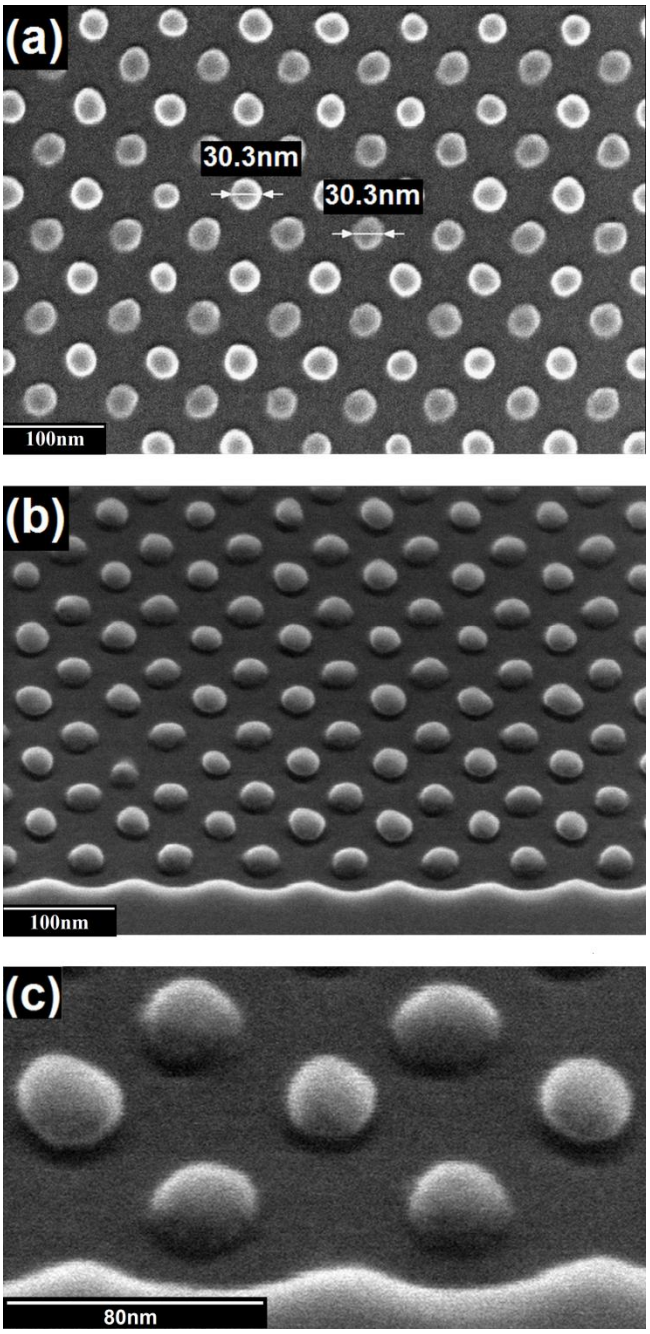

Figure 36: High magnification SEM images of density multiplication in an array of dots with a pre-multiplication pitch of 80 nm. The PMMA layer with an initial thickness of 43 nm on Si substrate was exposed with 1 keV voltage at a dose of 12.5 fC/dot and developed for 5 sec at -15°C; (a) plan view; (b) view at a 45° angle (c) inset of structures and sidewall from Figure (b), viewed at a 45° angle.

mixture for 5 sec at -15°C. Figure 36 (b) shows a perspective view of the same nanostructure shown in Figure 36 (a).

As can be seen in Figures 35 (a-d) and Figure 36 (a), features generated by partially exposed undeveloped resist are brighter than those which arise from cross-linking. One possible interpretation is that the features are different in height. However, from SEM image taken at a 45° angle (Figure 36 (b)) it is not evident that there is any significant difference between the heights of the features from positive-tone and negative-tone responses of PMMA. The higher magnification SEM micrograph in Figure 36 (c), which is a zoomed inset from Figure 36 (b), further suggests that one can expect rather similar heights of the features. Therefore, the difference in brightness is possibly due to higher carbon content in cross-linked spots as a result of carbonization caused by intense irradiation, which apparently reduces the emission of electrons from negative-tone PMMA [22, 34, 41, 95] and the angular fraction of the secondary electrons being collected under different observation angles. [95]

Figure 37 (a) shows a high magnification plan view SEM micrograph of density multiplication in PMMA gratings fabricated using an initially 100 nm pitch array of lines in a 43 nm thick layer of PMMA on a Si substrate, exposed with 1 keV electrons at a dose of 2000 pC/cm, and developed in MIBK:IPA 1:3 mixture for 5 sec at -20° C. Figure 37 (b) shows a 70° angle view of the same nanostructures. Similarly to the dots pattern in Figure 36, the brightness of the features resulting from positive-tone and negative-tone responses of PMMA is different, which is

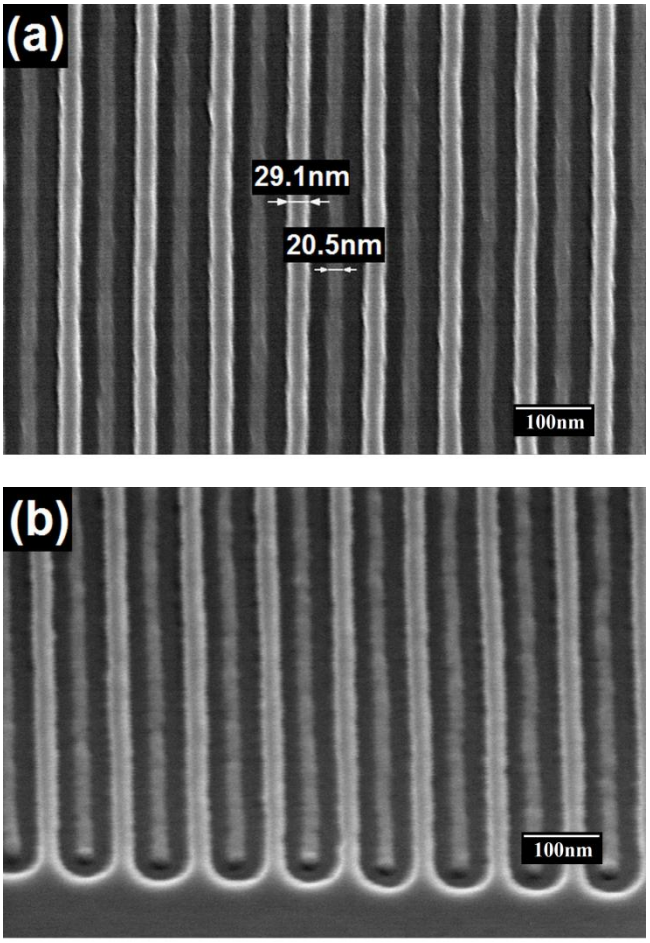

Figure 37: SEM images of density multiplication in an array of lines with a pre-multiplication pitch of 100 nm. The PMMA layer with an initial thickness of 43 nm on Si substrate was exposed with 1 keV voltage at the dose of 2000 pC/cm and developed for 5 sec at -20°C; (a) plan view and (b) 70° angled view.

attributable to a difference in chemical composition, particularly carbonization, [22, 34] as a result of the high exposure of the PMMA.

The nanostructures with density multiplication shown in Figure 35 (c), Figure 36 (a), and Figure 37 (a) were characterized by size measurements using the metrology capability of the Quartz PCI software. For initially 100 nm pitch dots (Figure 35 (c)), fabricated with a 33.3 fC/dot dose, the measured diameter was

approximately 37.9 ± 2.6 nm for both negative-tone and positive-tone PMMA response, and in the array of initially 80 nm pitch dots obtained with the dose of 12.5 fC/dot (Figure 36 (a)) the diameter of all dots was approximately 30.6 ± 1.8 nm for both negative-tone and positive-tone PMMA. For initially 100 nm pitch gratings written with the dose of 2000 pC/cm as shown in Figure 37 (a), the width of the lines from positive-tone and negative-tone response was somewhat different; in the second case, the measured line width was found to be approximately 21.5 ± 0.6 nm.

In order to better understand the conditions of exposure in PMMA required to achieve the density multiplication, numerical modeling of exposure was carried out using our recently developed EBL simulation tool [12]. The insight gained from such a study could be useful in predicting and optimizing density multiplication for various geometries and process conditions. Figure 38 (a-c) present the actual levels of the nominal yield of scission per monomer in a periodic dot pattern in PMMA. The exposure conditions were similar to those for Figure 34, which is close to the experimental design illustrated by Figure 35 (a). Figure 38 (a) and Figure 38 (b) illustrate the lateral dependencies of the yield of the scission at the top and at the bottom of the PMMA layer, respectively; whereas Figure 38 (c) shows the depth dependence of the yield in an exposed spot. Scission yields larger than 1 in Figures 38 (a-c) indicate that inelastic collisions of electrons with PMMA are more abundant than required to break the resist into monomers. It is clear from Figure 38 that there is a very strong exposure of the polymer at the top of the resist; however the strongest exposure is confined to a very narrow spot, for

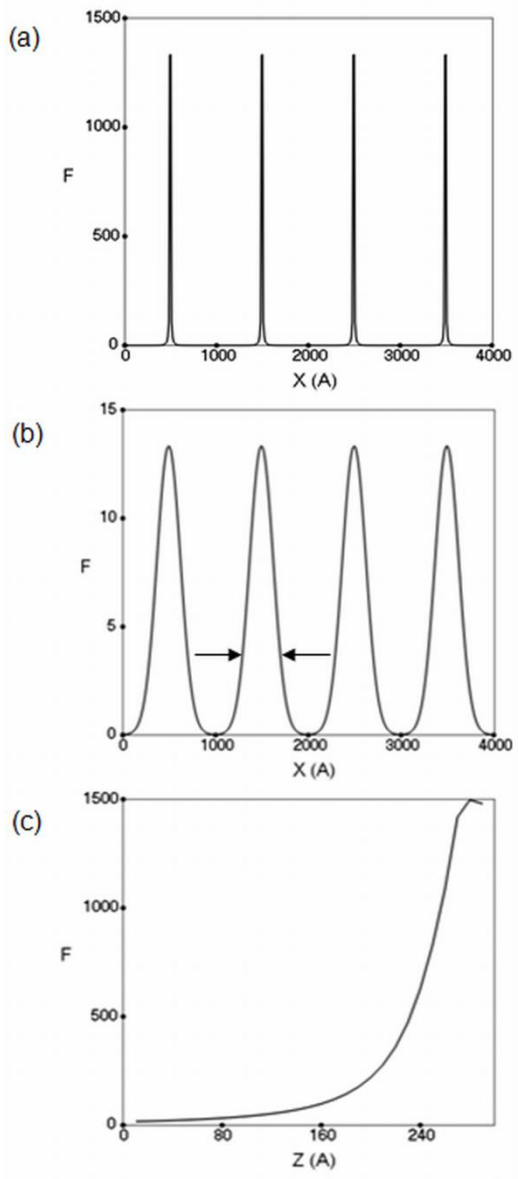

Figure 38: Plots of the predicted nominal yield of scissions per monomer of PMMA for a periodic array of 100 nm pitch dots in an initially 30 nm thick layer of PMMA on a Si substrate, exposed with 1 keV voltage and a point dose of 33.3 fC/dot; (a) the dependence on the lateral position at the top of the resist; (b) the dependence at the bottom of the resist; (c) the dependence on depth in an exposed spot. In (a) and (b), X is the lateral coordinate, and in (c), Z=0 corresponds to the bottom of the resist. The dimensions are in angstroms. In (b), the arrows indicate the level of scission corresponding to a width of 37.9 nm, corresponding to the observed diameter of the cross-linked spot at similar conditions.

which reason the topmost layers of the resist are not expected to contribute significantly to the formation of cross-linked nanostructures. At the bottom of the substrate, the exposed spot is broadened because of elastic scattering of electrons. Despite relatively mild conditions of exposure in this area, one can expect that the regions interfacing the substrate would determine the lateral size and overall robustness of the cross-linked structures. We therefore employed the lateral dependence of the scission yield at the bottom of the resist (Figure 38 (b)) to determine the nominal level of scissions that could correspond to the experimentally observed diameters of the cross-linked spots. The arrows in Figure 38 (b) indicate the width of 37.9 nm, corresponding to the observed diameter of the cross-linked spot at similar conditions of exposure. The corresponding yield of scission per monomer is approximately 3.6.

Figure 39 shows the nominal yield of scissions per monomer in a grating with initially 100 nm pitch lines simulated with 1 keV exposure and dose of 2000 pC/cm in an 43 nm thick layer of PMMA on a Si substrate. These exposure conditions are similar to the experiments where density multiplication was obtained (see Figure37). Qualitatively, the predicted trends are similar to the periodic dot pattern: a very strong exposure occurs in a limited area at the top of the resist, whereas at the bottom, the yield of scissions is less and the distributions are significantly broader. At the same time, although both Figure 39 and Figure 38 represent the conditions of dose multiplication, the maximal levels of scission in lines and dots differ significantly. From comparison of Figures 38 and 39, it is clear that, depending on the depth, the scission yields in the middle of the exposed

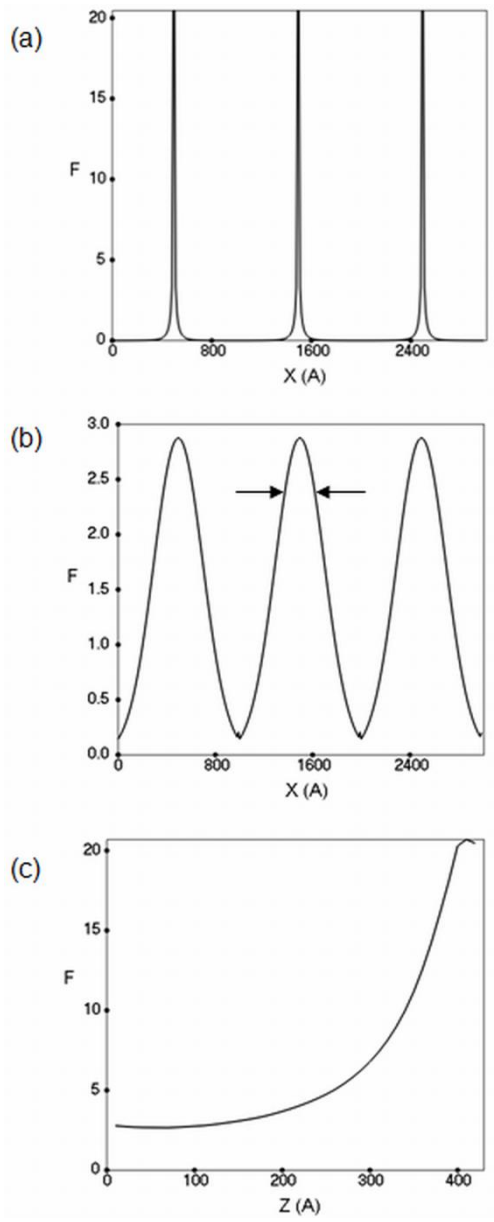

Figure 39: Plots of the predicted nominal yield of scissions per monomer for the case of 100 nm pitch single pixel lines (periodic grating) in an initially 43 nm thick layer of PMMA on a Si substrate, exposed with 1 keV voltage and a line dose of 2000 pC/cm: (a) the dependence on the lateral position at the top of the resist (b) the dependence at the bottom of the resist; (c) the dependence on depth for an exposed line. The dimensions are in angstroms. In (b), the arrows indicate the level of scission corresponding to a width of 21.5 nm, corresponding to the observed diameter of the cross-linked spot at similar conditions.

dots are from 5 to almost 70 times higher than in the lines. However, analysis of the yield of scission corresponding to the experimentally observed width of the lines (21.5 nm) revealed the yield value of approximately 2.5, which is the same order of magnitude as the value of 3.6 determined for dots. We conclude that in both dot patterns and gratings, PMMA responds as a negative tone resist at the locations where the nominal yield of scission per monomer approaches or exceeds the level of 2-3. This level of exposure appears to be somewhat less in lines than in dots, which is attributable to the geometrical factor: extended geometry of lines allows for more robust cross-linked structures than possible in dots at similar local conditions of exposure. Another observation is that, in order to reach the required level of scissions of 2-3 at the bottom of the resist, significantly higher exposure doses per pixel are required in single-pixel dot patterns than in single-pixel line patterns. Such numerical predictions can be employed to design other density multiplication EBL designs, some of which are demonstrated below.

In comparison to the direct-write approach of fabrication of nanostructures, it is clear that density multiplication using ultra-low voltages presents advantages, first, because of increased throughput since an initial periodic pattern of structures as shown in Figure 17 (a, b) is converted to a periodic pattern of higher density as shown in Figure 36 and Figure 37, respectively. Using a direct-write approach on PMMA as a negative-tone resist alone, a pattern of similar density would obviously require more time for exposure. The improvement in throughput obtained in this work is in terms of the increase in the number of features generated as well as the lower electron dose due to increased sensitivity of

PMMA at ultra-low voltages. In comparison to reverse-tone arrays of pits of a comparable pitch fabricated in PMMA by direct-write EBL with 30 keV exposures, [96] the density multiplication employing 1 keV exposures provides a comparable quality of patterns. The present approach of density multiplication, which has been used for initially 100 nm pitch arrays of dots and gratings, could be used to write patterns with smaller pitches by choosing an initial smaller pitch pattern and controlling the exposure dose and thickness of the resist. Because ultra-low voltage exposures are employed, the computationally intensive and time consuming proximity correction optimization is not required for this method. Considering recent findings suggesting that another polymeric resist with enhanced etch durability, ZEP, can perform in both positive and negative tone regimes [97] one can expect to fabricate dense patterns for usage as etch masks.

Figure 40 shows SEM images of cross and T-junction patterns formed by arrays of single pixel lines with an initial pitch of 100 nm, fabricated in a 43 nm thick PMMA layer on Si substrate, exposed with 1 keV voltage and developed in MIBK:IPA 3:1 mixture for 5 sec at -20°C. In Figure 40 (a), the plan view of a cross structure fabricated using a line dose of 2000 pC/cm is shown, and Figure 40 (b) shows a higher magnification 70° angled SEM image of the nanostructures resulting from cross-linked and undeveloped PMMA in the junction area. Figure 40(c) shows a plan view of the T-junction structure area showing density multiplication at a dose of approximately 2000 pC/cm, and Figure 40 (d) shows a 70° angle view of the T-Junction area illustrating the density multiplication at a dose of 2000 pC/cm. The SEM micrographs in Figure 40 show both positive-tone

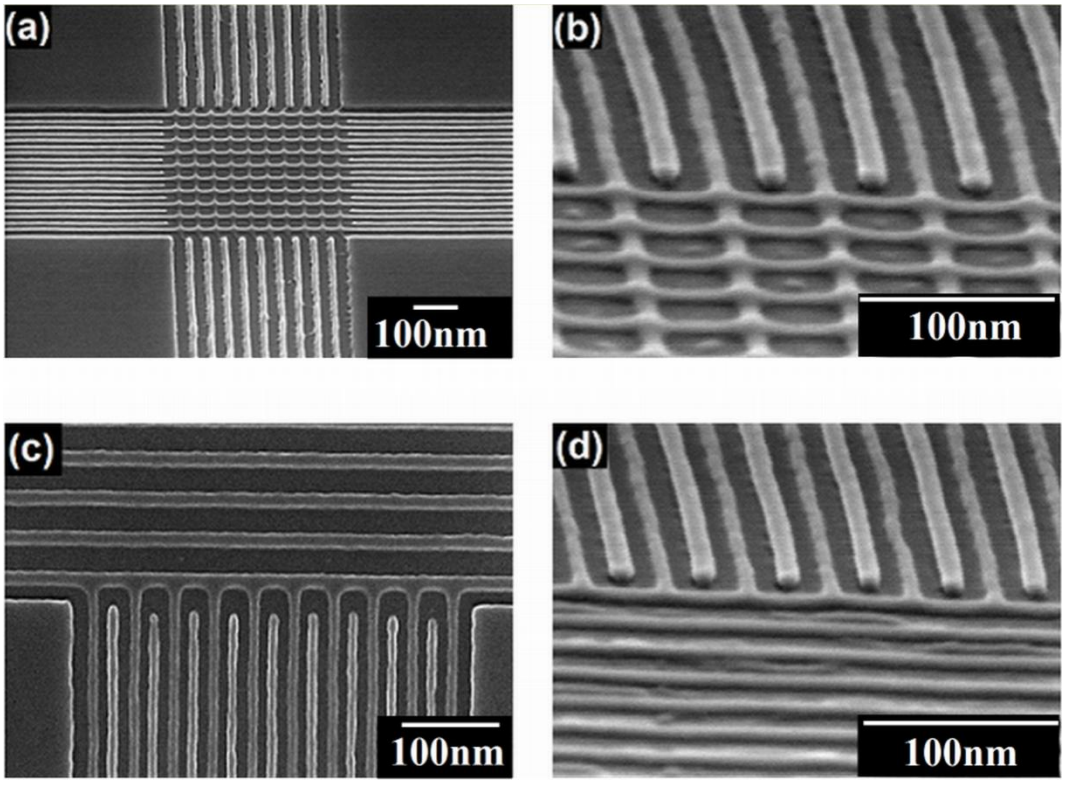

Figure 40: SEM images of density multiplication in cross and T-junction nanostructures formed by single pixel lines with an initial pitch of 100 nm. The nanostructures were fabricated in an initially 43 nm thick PMMA layer on Si substrate, exposed with 1 keV and developed in MIBK:IPA 3:1 mixture for 5 sec at -20°C; (a) plan view of cross structure; (b) higher resolution 70° angle view of cross structure; (c) plan view of T-junction structure showing density multiplication at the junction area; and (d) 70° angle view of T-junction structures showing density multiplication at the junction area.

and negative-tone lines; however in Figure 40 (b), the intersection part of the image contains mostly negative-tone lines. Because of stronger exposure in this area, most of the positive-tone PMMA has been removed (over-exposed) and only small residuals of undeveloped PMMA are visible. By carefully selecting the exposure dose, the residues can be eliminated. In the junction region of Figure 40 (d), while the array of vertically aligned lines exhibit well-exposed periodic

positive-tone and negative-tone PMMA gratings, the horizontally aligned gratings show negative-tone PMMA gratings (with slight under-exposure) and residues of partially exposed PMMA which were incompletely removed during development leaving residual PMMA. The difference in the morphologies of these structures is caused by a slight non-uniformity of exposure between vertically and horizontally aligned features, and can also be eliminated by a careful selection of the exposure conditions. The results described in this article demonstrate that the present methodology of density multiplication has a potential and flexibility for diverse applications with various writing designs.

6 Conclusion and Future Work

The potential of EBL is very promising and further development to a parallel process, rather than a serial process, is believed to possibly hold the key to high volume manufacturing. For this to be achieved, continuous research and development is necessary to optimize the process, create novel materials and integrate the knowledge to create the devices of the future. Both experimentation and numerical modeling of EBL processes assist in complex optimization of process parameters such as the exposure voltage, electron dose, development time and development temperature, which is required to achieve deep nanoscale resolution.

This thesis describes my contributions to ongoing research by experimentation and simulation in the Nanofabrication at the Department of Electrical and Computer Engineering of the University of Alberta. The conclusions and summary of my work as well as ideas for future research are outlined below:

1. EBL Nanofabrication of structures at ultra-low energy exposures of 1 keV and 2 keV, although challenging, is viable and presents a number of advantages over mid to high energy regimes.

2. At least three process parameters (the exposure dose, development time, and temperature) are found to be critical for the quality of the resist pattern and for optimal results of the EBL process, these parameters should be carefully selected. Understanding dose windows is particularly important at such low energies.

3. Certain trends established earlier for 3, 10 and 30 keV are applicable and relevant at low-keV regimes. Specifically, the trend of the dose window as a function of development time shows that longer development also reduces the dose window at low-keV. In addition, it has also been established that in agreement with previous work that denser structures have reduced dose windows. While a bigger process latitude is available at 80 nm pitch gratings, it contracts at 60 nm pitch.

4. In agreement with previous work, increasing the energy from 1 keV to 2 keV increased the dose window.

5. Cold development significantly increases the resolution of low-keV exposure and presents a very viable process window.

6. At ultra-low voltages of 1 keV, special regimes were found to exist when positive and negative tone PMMA coexist resulting in pattern density multiplication of nanopatterns in a single exposure-development step.

7. This work made extensive use of our EBL simulator for in-silico identification of initial process conditions, which were made available by the simulations. The simulations played a significant role in the complex optimization of several process parameters which are impossible to predict otherwise.

8. A degree of non-uniformity of exposure was observed with the patterning tool at the ultra-low energies. An improvement can be reached by reducing the beam step size, reducing the size of the write field and ensuring that

patterns are placed closer to the center of the beam axis than to the boundaries of the write field.

9. In the future, more detailed work could be done to study the quality of patterns written with the same dose across the entire write field. This would give a more uniform qualitative measure of the severity of the exposure variation issue in the patterning tool.

10. The density multiplication work is promising and replicating the effect with other resists such as ZEP would provide opportunities for further study both experimentally and through modeling.

References

[1] Semiconductor Industry Association (SIA), 2011, "Semiconductor Industry Reports January Chip Sales Grew 14.0% Year Over Year," Press release, www.sia-online.org (June 6, 2011).

[2] C. Kazmierski, "Global Semiconductor Sales Hit Record $298.3 Billion in 2010", Semiconductor Industry Association, Press Release. http://www.reuters.com/, (Jan. 31 2011).

[3] C. Kazmierski, "Semiconductor Industry Ends 1st Quarter with Strong Global Sales", Semiconductor Industry Association, Press Release. http://www10.edacafe.com (May 2, 2011).

[4] Intel Corporation, "Moore s Law Made Real by Intel Innovations." Web article, http://www. intel.com/technology/mooreslaw/. Accessed June 16 (2011).

[5] A. A. Tseng, *Nanofabrication: Fundamentals and Applications*: World Scientific Publishing Company, (2008).

[6] M. J. Madou, *Fundamentals of Microfabrication : the science of miniaturization*: CRC Press (2002).

[7] J. K. W. Yang, Y. S. Jung, J. Chang, R. A. Mickiewicz, A. Alexander-Katz, C. A. Ross, and K. K. Berggren, Nat. Nanotechnol. **5**, 256 (2010).

[8] S. Ji, C. Liu, G. Liu, and P. F. Nealey, ACS Nano **4**, 599 (2010).

[9] M. A. Mohammad, T. Fito, J. Chen, S. Buswell, M. Aktary, S. K. Dew, and M. Stepanova, In: Lithography, Michael Wang (Ed.) 293, (INTECH, 2010).

[10] M.A. Mohammad M. Mustafa, S. K. Dew, M. Stepanova, In: Nanofabrication Techniques and Principles, M. Stepanova and S. Dew (Eds.), 350, (Springer, 2012).

[11] M.A. Mohammad, S.K. Dew, K. Westra, P. Li, M. Aktary, Y. Lauw, A. Kovalenko, and M. Stepanova, J. Vac. Sci. Technol. B **25**, 745 (2007).

[12] M. Stepanova, T. Fito, Z. Szabo, K. Alti, A. P. Adeyenuwo, K. Koshelev, M. Aktary and S. K. Dew, J. Vac. Sci. Technol. B **28**, C6C48 (2010).

[13] M. Aktary, M. Stepanova and S. K. Dew, J. Vac. Sci. Technol. B, **24**, 768 (2006).

[14] W. Wu, W. M. Tong, J. Bartman, Y. Chen, R. Walmsley, et al., Nano Lett. **8**, 3865 (2008).

[15] Hitachi Global Storage Technologies, "Density Multiplication and Improved Lithography by Directed Block Copolymer Assembly for Patterned Media at 1 Tbit/in and Beyond", Hitachi GST, White Paper, www.hitachiGST.com (2008).

[16] B. D. Terris and T. Thomson, J. Phys. D, **38**, R199 (2005).

[17] I. Bita, J. K. Yang, Y. S. Jung,C. A. Ross, E. L. Thomas, K. K. Berggren, Science **321**, 939 (2008).

[18] J. K. Yang, A. J. Kerman, E. A. Dauler, et al., Appl. Supercond., IEEE Transactions **19**, 318 (2009).

[19] Z. Chen, Y. M. Lin,M. J. Rooks, P. Avouris, PHYSICA E **40**, 228 (2007).

[20] R. Ruiz, H. Kang, F. A. Detcheverry, E. Dobisz, D. S. Kercher, T. R. Albrecht, J. J. de Pablo, and P. F. Nealey, Science **321,** 936 (2008).

[21] B. Cord, J. Lutkenhaus and K. K. Berggren, J. Vac. Sci. Technol. B **25**, 2013 (2007).

[22] H. Duan, D. Winston, J.K.W. Yang, B.M. Cord, V. R. Manfrinato, K.K. Berggren, J. Vac. Sci. Technol. B **28**, C6C58 (2010).

[23] Mapper Lithography, "MAPPER technology." Web Article, http://www.mapperlithography.com/technology-mapper.html/. Accessed November 11, (2011).

[24] L. P. Muray, J. P. Spallas, C. Stebler, K. Lee, M. Mankos, Y. Hsu, M. Gmur, and T. H. P. Chang, J. Vac. Sci. Technol. B **18**, 3099 (2000).

[25] T. H. P. Chang, D. P. Kern, and L. P. Muray, J. Vac. Sci. Technol. B **10**, 2743 (1992).

[26] A. Jamieson, C. Willson, Y. Hsu and A. Brodie, J. Microlithogr. Microfabrication, Microsyst. **3**, 442 (2004).

[27] International Technology Roadmap for Semiconductors, ITRS 2009 Edition

Lithography." Web Article http://www.itrs.net/Links/2009ITRS/2009Chapters_2009Tables/2009_Litho.pdf Accessed October 1 (2011).

[28] Y. Lee, R. Browning, N. Maluf, G. Owen and R. Pease, J. Vac. Sci. Technol. B **10**, 3094 (1992).

[29] K. D. Schock, F. E. Prins, S. Strahle and D. P. Kern, J. Vac. Sci. Technol. B **15**, 2323 (1997).

[30] M. A. Mohammad, T. Fito, J. Chen, S. Buswell, M. Aktary, M. Stepanova, and S. K. Dew, Microelectronic Engineering, **87**, 1104 (2010).

[31] I. Zailer, J. E. F. Frost, V. Chabasseur-Molyneux, C. J. B. Ford, and M. Pepper, Semicond Sci Tech. **11**, 1235 (1996)

[32] M. A. Mohammad, T. Fito, J. Chen, M. Aktary, M. Stepanova, and S. K. Dew, J. Vac. Sci. Technol. B. **28**, L1 (2010).

[33] W. Hu, K. Sarveswaran, M. Lieberman, and G. H. Bernstein, J. Vac. Sci. Technol. B. **22**, 1711 (2004).

[34] H. Duan, J. Zhao, Y. Zhang, E. Xie, and L. Han, Nanotechnology **20**, 135306 (2009).

[35] H. G. Duan, E. Xie, L. Han, and X. Zhi, Adv. Mater. **20**, 3284 (2008).

[36] S. Borini, J. Electrochem. Soc. **152**, G482 (2005).

[37] W.H. Teh and C.G.Smith, J. Vac. Sci. Technol. B **21**, 3007 (2003).

[38] A. C. F. Hoole, M E. Welland, and A. N. Broers, Semicond. Sci. Tech. **12**, 1166 (1997).

[39] H. G. Duan, E. Q. Xie, and L. Han, J. Appl. Phys. **103**, 046105 (2008).

[40] S. Gautsch, M. Studer, and N. F. de Rooij, Microelectron. Eng. **87**, 1139 (2010).

[41] S. Gautsch and N. F. de Rooij, Microelectron. Eng. **88**, 2533 (2011).

[42] Anner GE, *Planar Processing Primer:* Van Norstrand Reinhold (1990).

[43] Rai-Choudhury P. *SPIE Handbook of Microlithography, Micromachining and Microfabrication: Volume 1: Microlithograpy*: SPIE-International Society for Optical Engineering (1997).

[44] D. M. Tanenbaum, C. W. Lo, M. Isaacson, H. G. Craighead, M. J. Rooks, K. Y. Lee, W. S. Huang and T. H. P. Chang, J. Vac. Sci. Technol. B **14**, 3829 (1996).

[45] H. Yang, L. Fan, A. Jin, Q. Luo, C. Gu, and Z. Cui, Proc. 1st IEEE-NEMS, **60501014**, 391 (2006).

[46] N. Clark, A. Vanderslice, R. Grove III and R. R. Krchnavek, J. Vac. Sci. Technol. B **24**, 3073 (2006).

[47] J. Fujita J, Y. Ohnishi, Y. Ochiai, S. Matsui, Appl Phys Lett. **68**, 1297 (1996).

[48] A. Tilke, M. Vogel, F. Simmel, A. Kriele, R. H. Blick, H. Lorenz, D. A, Wharam, J.P. Kotthaus. J. Vac. Sci. Technol. B. **17**, 1594 (1999).

[49] H. Namatsu, T. Yamaguchi, and K. Kurihara, Mat. Res. Soc. Symp. Proc., **584**, 135 (2000).

[50] V. M. Bermudez, J. Vac. Sci. Technol. B. **17**, 2512 (1999).

[51] D. C. Joy, *Monte Carlo Modeling for Electron Microscopy and Microanalysis:* Oxford University Press (1995).

[52] B. K. Paul, Microelectron Eng, **49**, 233 (1999).

[53] I. Raptis, N. Glezos and M. Hatzakis, J. Vac. Sci. Technol. B **11**, 2754 (1993).

[54] Schmoranzer H and Reisser M, Nucl. Instrum. Meth. B, **105**, 35 (1995).

[55] I. Raptis, N. Glezos, E. Valamontes, E. Zervas, and P. Argitis, Vacuum, **62**, 263 (2001).

[56] Vutova K., In: Lithography, Michael Wang (Ed.) 319, (INTECH, 2010).

[57] I. Adesida, R. Shimizu and T. Everhart, J. Appl. Phys. **51**, 5962 (1980).

[58] D. Kyser and N. Viswanathan, J. Vac. Sci. Technol. **12**, 1305-4 (1975).

[59] Y. Lee, W. Lee, K. Chun and H. Kim, J. Vac. Sci. Technol. B **17**, 2903 (1999).

[60] C. Marrian, F. Perkins, D. Park, E. Dobisz, M. Peckerar, K. Rhee and R. Bass, J. Vac. Sci. Technol. B **14,** 3864 (1996).

[61] R. Shimizu and T. Everhart, Appl. Phys. Lett. **33,** 784 (1978).

[62] J. Goldstein, D. E. Newbury, D. C. Joy, C. E. Lyman, P. Echlin, E. Lifshin, L. Sawyer and J. R. Michael, *Scanning Electron Microscopy and X-ray Microanalysis,* 3rd edition, New York: Springer (2007).

[63] CASINO, monte Carlo Simulation of electron trajectory in sOlids." Web Article, http://www.gel.usherbrooke.ca/casino/. Accessed October 1, (2011).

[64] Institute for National Measurement Standards, "EGSnrc." Web Article http://irs.inms.nrc.ca/software/egsnrc/. Accessed October 1, (2011).

[65] CHARIOT, "ABeam Technologies." Web Article http://www.abeamtech.com/?dir=products/CHARIOT&pg=details. Accessed October 1, (2011).

[66] National Institute for Science and Technology, "NISTMonte." Web Article http://www.cstl.nist.gov/div837/837.02/epq/index.html. Accessed October 1, (2011).

[67] National Institute for Science and Technology, "NIST DTSA-II." Web Article http://www.cstl.nist.gov/div837/837.02/epq/dtsa2/index.html. Accessed October 1, (2011).

[68] H. Demers, “Win X-Ray - Electron Beam Scattering Modeling.” Web Article http://montecarlomodeling.mcgill.ca/software/winxray/winxray.html. Accessed October 1, (2011).

[69] Nuclear Energy Agency. “PENELOPE2011, A Code System for Monte-Carlo Simulation of Electron and Photon Transport.” Web Article http://www.oecd-nea.org/tools/abstract/detail/nea-1525. Accessed October 1, (2011).

[70] D. C. Joy. “Monte Carlo Simulation.” Web Article http://web.utk.edu/~srcutk/htm/simulati.htm. Accessed October 1, (2011).

[71] Small World. “Electron Flight Simulator.” Web Article http://www.small-world.net/efs.htm. Accessed October 1, (2011).

[72] MC-SET, “MC-SET - Monte Carlo Simulation of Electron Trajectories.” Web Article, http://www.mc-set.com/. Accessed October 1, (2011).

[73] NINT Electron Beam Lithography Simulator, Manual and Case Studies, (National Institute for Nanotechnology and University of Alberta, Edmonton, AB, Canada, 2010), 40 p.

[74] Flintbox, “NINT Electron Beam Lithography Simulator”, http://www.flintbox.com/public/project/7272/. Accessed October 1, (2011).

[75] M.A. Mohammad, Zs. Szabó, T. Fito, J.M. Lee, J. Chen, M. Aktary, S. K. Dew, M. Stepanova, *Nanotech 2009 – 2009 NSTI Nanotechnology Conference and*

Expo (Houston, 2009).

[76] N. Glezos, I. Raptis, D. Tsoukalas, and M. Hatzakis, J. Vac. Sci. Technol. B **10**, 2606 (1992).

[77] N. Glezos and I. Raptis, IEEE Trans. CADICS, **15**, 92 (1996).

[78] P.-F. Staub, J. Phys. D **27**, 1533 (1994).

[79] A. Jablonski, J. Gryko, J. Kraaser, and S. Tougaard, Phys. Rev. B **39**, 61 (1989).

[80] E. W. Montroll and R. Simha, J. Chem. Phys. **8**, 721 (1940).

[81] W. Kuhn, Ber. Dtsch. Chem. Ges. B **63**, 1503 (1930).

[82] B.A. Miller-Chou, J.L. Koenig, Prog. Polym. Sci. **28**, 1223 (2003).

[83] L. Masaro, X.X. Zhu, Prog. Polym. Sci. **24**, 731 (1999).

[84] Zs. Szabo, National Institute for Nanotechnology Report (2009).

[85] OpenGL, "The Industry's Foundation for High Performance Graphics." Web Article, http://www.opengl.org/documentation/. Accessed November 10, (2011).

[86] TIFF, "TIFF Revision 6.0 - Adobe Partners." Web Article, http://partners.adobe.com/public/developer/tiff/index.html/. Accessed November 10, (2011).

[87] Gnuplot, "gnuplot homepage." Web Article http://www.gnuplot.info/. Accessed

November 10, (2011).

[88] V. Wiaux, G. Storms, S. Cheng, and M. Maenhoudt, "The potential of double patterning immersion lithography for the 32nm half pitch node", EuroAsia Semiconductor, Lithography, Web article, http://www.euroasiasemiconductor.com/print_version.php?id=69951 (2007).

[89] M. Maenhoudt, R. Gronheid, N. Stepanenko, T. Matsuda and D. Vangoidsenhoven, SPIE **6924,** 69240P (2008).

[90] A. Carlson and T. K. Liu, Proc. Proc. SPIE **6924,** 1 (2008).

[91] B. Degroote, R. Rooyackers, T. Vandeweyer, N. Collaert, W. Boullart, E. Kunnen, D. Shamiryan, J. Wouters, J. Van Puymbroeck, A. Dixit, and M. Jurczak, Microelectron. Eng. **84**, 4 (2007)

[92] S. Song, S. Yokoyama, S. Takahara, and T. Yamaoka, Poly. for Adv. Tech. **9,** 6 (1998).

[93] C. Fonseca, M. Somervell, S. Scheer, W. Printz, K. Nafus, S. Hatakeyama, Y. Kuwahara, T. Niwa, S. Bernard, and R. Gronheid, Proc. SPIE **7274,** 1 (2009).

[94] C. Fonseca, M. Somervell, S. Scheer, Y. Kuwahara, K. Nafus, R. Gronheid, S. Tarutani, and Y. Enomoto, Proc. SPIE **7640,** 1 (2010).

[95] Z. Tan, Y. Xia, X. Liu, and M. Zhao, Microelectron. Eng. **77**, 285 (2005).

[96] M. A. Mohammad, Cs. Guthy, S. Evoy, S. K. Dew, and M. Stepanova, J. Vac. Sci. Technol. B **28**, C6P36 (2010).

[97] J. Cazeaux, Ultramicroscopy **110**, 242 (2010).

[98] M. Muhammad, S. C. Buswell, S. K. Dew, and M. Stepanova, J. Vac. Sci. Technol. B **29**, 06F304 (2011).

[99] T. G. Oyama, A. Oshima, H. Yamaoto, S. Tagawa, and M. Washio, Appl. Phys. Express **4**, 076501 (2011).